Article

Cancer Cell

Targeting the Vulnerability of Glutathione Metabolism in ARID1A-Deficient Cancers

Graphical Abstract

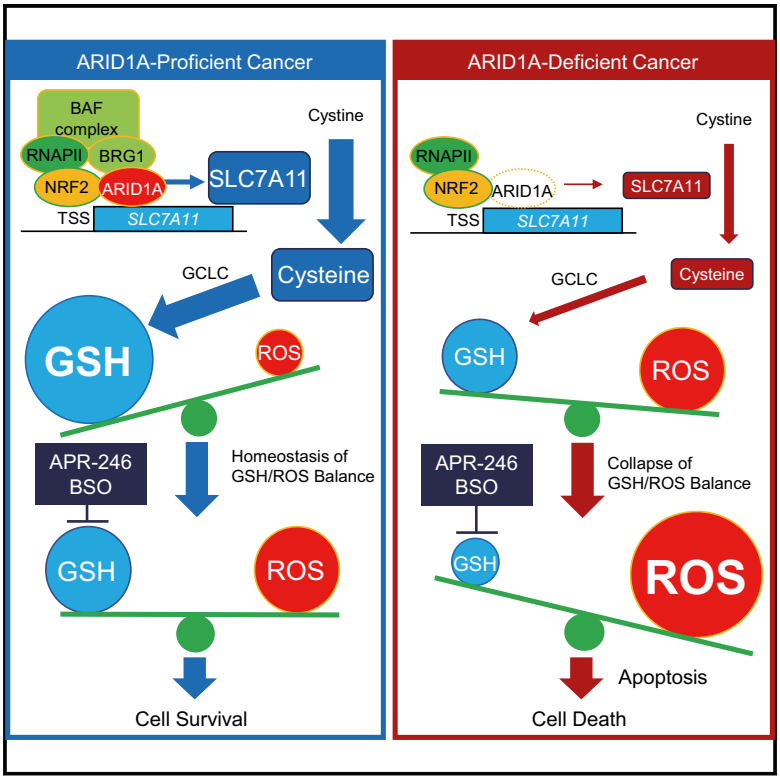

Highlights

- ARID1A maintains GSH homeostasis by enhancing *SLC7A11* transcription
- Low SLC7A11 expression causes low basal GSH levels in ARID1A-deficient cancer cells
- Inhibiting GSH/GCLC in ARID1A-deficient cancer cells causes apoptosis by ROS
- GCLC is a druggable synthetic lethal target for ARID1A-deficient cancer

Authors

Hideaki Ogiwara, Kazuaki Takahashi, Mariko Sasaki, ..., Tomoyasu Kato, Aikou Okamoto, Takashi Kohno

Correspondence

hogiwara@ncc.go.jp (H.O.), tkkohno@ncc.go.jp (T.K.)

In Brief

Ogiwara et al. show that ARID1A-deficient cancer cells express low levels of the key cystine transporter SLC7A11 and thus have low basal levels of glutathione (GSH), which make these cancer cells specifically vulnerable to inhibition of the GSH metabolic pathway.

Ogiwara et al., 2019, Cancer Cell *35*, 177–190
February 11, 2019
https://doi.org/10.1016/j.ccell.2018.12.009

CellPress

Cancer Cell
Article

Targeting the Vulnerability of Glutathione Metabolism in ARID1A-Deficient Cancers

Hideaki Ogiwara,[1,9,*] Kazuaki Takahashi,[1,2,9] Mariko Sasaki,[1,3] Takafumi Kuroda,[1,2] Hiroshi Yoshida,[4] Reiko Watanabe,[4] Ami Maruyama,[5,6] Hideki Makinoshima,[5] Fumiko Chiwaki,[7] Hiroki Sasaki,[7] Tomoyasu Kato,[8] Aikou Okamoto,[2] and Takashi Kohno[1,3,10,*]

[1]Division of Genome Biology, National Cancer Center Research Institute, 5-1-1, Tsukiji, Chuo-ku, Tokyo 104-0045, Japan
[2]Department of Obstetrics and Gynecology, The Jikei University School of Medicine, 3-25-8 Nishi-Shinbashi, Minato-ku, Tokyo 105-8461, Japan
[3]Molecular Oncology, The Jikei University Graduate School of Medicine, 3-25-8 Nishi-Shinbashi, Minato-ku, Tokyo 105-8461, Japan
[4]Department of Pathology and Clinical Laboratories, National Cancer Center Hospital, 5-1-1, Tsukiji, Chuo-ku, Tokyo 104-0045, Japan
[5]Tsuruoka Metabolomics Laboratory, National Cancer Center, Tsuruoka, Yamagata 997-0052, Japan
[6]Shonai Regional Industry Promotion Center, Tsuruoka, Yamagata 997-0015, Japan
[7]Department of Translational Oncology, Fundamental Innovative Oncology Core Center, National Cancer Center Research Institute, 5-1-1, Tsukiji, Chuo-ku, Tokyo 104-0045, Japan
[8]Department of Gynecology, National Cancer Center Hospital, 5-1-1, Tsukiji, Chuo-ku, Tokyo 104-0045, Japan
[9]These authors contributed equally
[10]Lead Contact
*Correspondence: hogiwara@ncc.go.jp (H.O.), tkkohno@ncc.go.jp (T.K.)
https://doi.org/10.1016/j.ccell.2018.12.009

SUMMARY

ARID1A encodes an SWI/SNF chromatin-remodeling factor and is frequently mutated in various cancers. This study demonstrates that ARID1A-deficient cancer cells are specifically vulnerable to inhibition of the antioxidant glutathione (GSH) and the glutamate-cysteine ligase synthetase catalytic subunit (GCLC), a rate-limiting enzyme for GSH synthesis. Inhibition of GCLC markedly decreased GSH in ARID1A-deficient cancer cells, leading to apoptotic cell death triggered by excessive amounts of reactive oxygen species. The vulnerability of ARID1A-deficient cancer cells results from low basal levels of GSH due to impaired expression of *SLC7A11*. The *SLC7A11*-encoded cystine transporter supplies cells with cysteine, a key source of GSH, and its expression is enhanced by ARID1A-mediated chromatin remodeling. Thus, ARID1A-deficient cancers are susceptible to synthetic lethal targeting of GCLC.

INTRODUCTION

Current precision medicine for the treatment of advanced human cancer depends largely on targeting activated protein kinases using specific inhibitors or antibodies (Yoh et al., 2016). Only a fraction of cancers harbor such druggable kinase aberrations; therefore, the next generation of blockbuster anticancer therapeutics will be drugs that target non-kinase genetic aberrations, which constitute the majority of genetic aberrations in most cancer cells. Notably, some deleterious (loss-of-function) gene mutations confer druggable vulnerabilities on cancer cells. Synthetic lethality is defined by an interdependent relationship between two genes, which means that simultaneous loss of two genes, but not loss of either gene alone, leads to cell death. Cancer cells harboring a deleterious gene mutation would therefore be vulnerable to inhibition of the synthetic lethal target, as epitomized by the success of PARP1-targeted therapy against hereditary breast and ovarian cancers harboring *BRCA1* and *BRCA2* mutations (Lord and Ashworth, 2016). Thus, discovery of cancer vulnerabilities associated with frequent deleterious gene mutations could improve cancer therapy dramatically.

Significance

Deleterious *ARID1A* mutations are frequent in ovarian clear cell (50%) and ovarian endometrioid (30%) carcinoma and many other types of cancer, and there is no effective therapy targeting these mutations. We show that cultured and primary cancer cells lacking ARID1A protein expression have a common feature of low *SLC7A11* expression caused by impaired ARID1A-mediated transcriptional activation. Such ARID1A-deficient cancer cells were specifically vulnerable to inhibitors of the GSH metabolic pathway, such as APR-246 for GSH and buthionine sulfoximine for GCLC, due to the low supply of cysteine, a key source of antioxidant GSH. Therefore, GCLC-targeting therapy is promising for ovarian and other cancers lacking ARID1A expression.

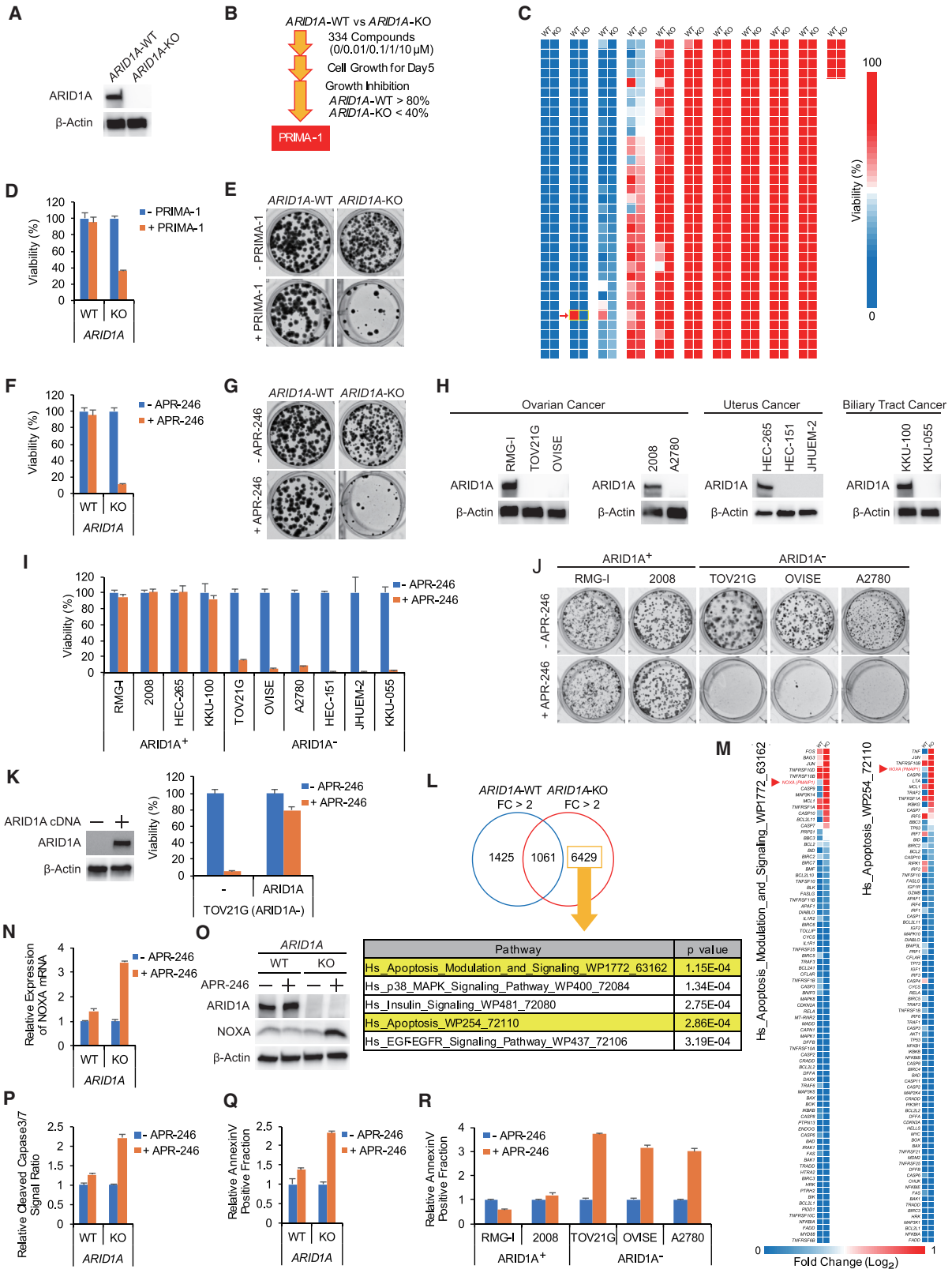

Figure 1. ARID1A-Deficient Cancer Cells Are Selectively Sensitive to PRIMA-1 and APR-246

(A) Immunoblotting for ARID1A and β-actin in whole-cell extracts of *ARID1A*-WT and *ARID1A*-KO HCT116 cells.

(B) Scheme showing screening for compounds that selectively suppress the growth of *ARID1A*-KO cells.

(legend continued on next page)

Regulation of oxidative stress homeostasis is important for cell survival. Reactive oxygen species (ROS) cause oxidative stress. Cellular ROS levels are determined by the balance between ROS generation and elimination, and are regulated by antioxidant defense mechanisms (Gorrini et al., 2013). High levels of ROS cause cell damage and death. Therefore, targeting antioxidant defense systems may be an anti-cancer therapeutic strategy. Glutathione (GSH) is an abundant antioxidant tripeptide molecule synthesized from cysteine, glutamate, and glycine by the ATP-dependent enzyme glutamate-cysteine ligase synthetase (GCL), which is composed of the glutamate-cysteine ligase catalytic subunit (GCLC) and the glutamate-cysteine ligase modifier subunit, and GSH synthetase (GSS) (Bin et al., 2017). GCL catalyzes the rate-limiting step of glutamate ligation with cysteine during GSH synthesis. Cysteine is the rate-limiting precursor substrate for GSH synthesis. Intracellular cysteine levels are controlled by *SLC7A11*, which encodes the cystine/glutamate transporter XCT (Sasaki et al., 2002).

Deleterious mutations of genes encoding subunits of the SWI/SNF chromatin-remodeling complex are commonly found in more than 20% of all human cancers (Kadoch et al., 2013). Such mutations are thought to promote tumorigenesis by disturbing transcriptional homeostasis due to impairment of DNA repair and chromatin remodeling in transcribed genes. *ARID1A*, which encodes a component of the SWI/SNF chromatin-remodeling complex, is frequently mutated in multiple cancer types and contributes significantly to carcinogenesis independent of *TP53*. *ARID1A* is mutated in about 46% of ovarian clear cell carcinomas (OCCCs), 43% of uterine corpus endometrial carcinomas (endometrial endometrioid carcinoma), 33% of gastric carcinomas, 30% of ovarian endometrioid carcinomas, 28% of bladder carcinomas, 27% of cholangiocarcinomas, 15% of pancreatic carcinomas, 12% of lung adenocarcinomas, and 10% of colorectal carcinomas (Ding et al., 2018; Jones et al., 2010; Lawrence et al., 2014; Wiegand et al., 2010), all of which lack effective therapies. Inactivation of *ARID1A* is associated with poor prognosis of several types of cancer (Luchini et al., 2015). Thus, much effort has been devoted to identifying vulnerabilities associated with ARID1A deficiency (Caumanns et al., 2018). However, no efficient therapeutic strategy has been established. The goal of this study is to develop an effective therapeutic strategy for treating ARID1A-deficient cancers by identifying druggable targets.

RESULTS

ARID1A-Deficient Cancer Cells Are Selectively Sensitive to PRIMA-1 and APR-246

To investigate cellular vulnerabilities caused by ARID1A deficiency, we examined the differential sensitivities of parenta *ARID1A*-wild-type (*ARID1A*-WT) and *ARID1A*-knockout (*ARID1A*-KO) HCT116 colon cancer cells to 334 inhibitors whose targets have been elucidated. A drug-sensitivity screen identified PRIMA-1 (APR-017) (Figure 1A–1C, Table S1), which binds covalently to thiols in multiple polypeptides (Bykov et al., 2016), as a unique hit that reproducibly suppressed the growth of *ARID1A*-KO cells but not *ARID1A*-WT cells (Figure 1D). The selective sensitivity of *ARID1A*-KO cells to PRIMA-1 was validated by measuring cell survival in colony formation assays (Figures 1E and S1A). APR-246 (PRIMA-1^{Met}), a structural analog of PRIMA-1, has been tested in clinical trials of hematological and prostate cancers (Lehmann et al., 2012). APR-246 markedly decreased the survival of *ARID1A*-KO cells, but not *ARID1A*-WT cells (Figures 1F, 1G, and S1B). Next, we tested the sensitivity of various ARID1A-deficient cancer cells to APR-246 and PRIMA-1. This analysis used a panel of four ARID1A-proficient and six ARID1A-deficient cell lines (Figure 1H). ARID1A-deficient cancer cells were more sensitive to APR-246 than ARID1A-proficient cancer cells (Figures 1I and S1C–S1E). The selective sensitivity of ARID1A-deficient cancer cells to APR-246 was validated by measuring cell survival in colony formation assays (Figures 1J and S1F). Similar results were obtained in PRIMA-1 treatment (Figures S1G and S1H). The preferential lethality of APR-246 and PRIMA-1 in TOV21G ARID1A-deficient cancer cells was rescued by stable expression of the ARID1A cDNA (Figures 1K and S1I), confirming that ARID1A deficiency was

(C) Heatmap of the cell viability of *ARID1A*-WT and *ARID1A*-KO HCT116 cells after treatment with 334 compounds (each at 10 μM) for 5 days. A red arrow indicates results from PRIMA-1-treated samples.
(D) Cell viability of *ARID1A*-WT and *ARID1A*-KO HCT116 cells after treatment for 5 days with 3.7 μM PRIMA-1.
(E) Colony formation of *ARID1A*-WT and *ARID1A*-KO HCT116 cells after treatment for 10 days with 2.5 μM PRIMA-1.
(F) Cell viability of *ARID1A*-WT and *ARID1A*-KO HCT116 cells after treatment for 5 days with 3.7 μM APR-246.
(G) Colony formation of *ARID1A*-WT and *ARID1A*-KO HCT116 cells after treatment for 10 days with 2 μM APR-246.
(H) Immunoblotting for ARID1A and β-actin in whole-cell extracts of the indicated cell lines.
(I) Cell viability of cancer cell lines after treatment for 3 days with 11 μM APR-246.
(J) Colony formation of ovarian cancer cell lines after treatment for 14 days with 1 μM APR-246.
(K) Immunoblotting for ARID1A and β-actin in whole-cell extracts of ARID1A-deficient TOV21G cancer cells with or without ectopic expression of ARID1A cDNA (left) and cell viability of these cells after treatment for 3 days with 11 μM APR-246 (right).
(L) A Venn diagram showing the numbers of genes in *ARID1A*-WT and *ARID1A*-KO HCT116 cells with altered expression after treatment for 24 h with 40 μM APR-246 and the top five most enriched pathways among 6,429 genes with significantly altered expression in *ARID1A*-KO cells by WikiPathways database analysis.
(M) Gene expression profiles of two apoptosis-related pathways in *ARID1A*-WT and *ARID1A*-KO HCT116 cells after treatment for 24 h with 40 μM APR-246. Red arrowheads indicate the profile of the *NOXA* gene.
(N) Relative mRNA levels of *NOXA* in *ARID1A*-WT and *ARID1A*-KO HCT116 cells after treatment for 24 h with 20 μM APR-246.
(O) Immunoblotting for ARID1A, NOXA, and β-actin in whole-cell extracts of *ARID1A*-WT and *ARID1A*-KO HCT116 cells after treatment for 24 h with 40 μM APR-246.
(P) Detection of cleaved caspase-3/7-positive apoptotic cells in *ARID1A*-WT and *ARID1A*-KO HCT116 cells after treatment for 48 h with 10 μM APR-246.
(Q) Detection of Annexin V-positive apoptotic cells in *ARID1A*-WT and *ARID1A*-KO HCT116 cells after treatment for 48 h with 15 μM APR-246.
(R) Detection of Annexin V-positive apoptotic cells in ovarian cancer cell lines after treatment for 48 h with 50 μM APR-246.
Data in (D, F, I, K, N, P, Q, and R) are expressed as the mean ± SD. See also Figure S1 and Table S1.

responsible for sensitivity to these drugs, irrespective of the cellular context.

To explore the sensitivity of *ARID1A*-KO cells to APR-246, genome-wide expression profiling was conducted. A pathway analysis of 6,429 genes whose expression levels in *ARID1A*-KO cells, but not in *ARID1A*-WT cells, increased or decreased by more than 2-fold upon APR-246 treatment was performed to identify the pathways responsible for the sensitivity of *ARID1A*-KO cells to ARP-246 (Figure 1L). Pathways related to apoptosis were significantly ($p < 0.001$) enriched among these genes (Figure 1L). Notably, several key pro-apoptotic genes, including *NOXA*, were markedly upregulated in *ARID1A*-KO cells, but not in *ARID1A*-WT cells (Figure 1M). qRT-PCR analysis verified that mRNA expression of *NOXA* increased in APR-246-treated *ARID1A*-KO cells and ARID1A-deficient cancer cells (Figures 1N, S1J, and S1K). Concordantly, protein expression of NOXA increased specifically in APR-246-treated *ARID1A*-KO cells (Figure 1O). Moreover, APR-246 treatment induced apoptosis, as assessed by caspase activation and Annexin V appearance, in *ARID1A*-KO cells and ARID1A-deficient cancer cells (Figures 1P–1R, S1L, and S1M).

ARID1A-Deficient Cancer Cells Are Vulnerable to GSH Inhibition

APR-246 is converted to the Michael acceptor methylene quinuclidinone (MQ), which inhibits activity of the antioxidant metabolite GSH and the antioxidant regulator thioredoxin reductase (TrxR) by reacting with their thiols (Peng et al., 2013; Tessoulin et al., 2014). Covalent binding of MQ decreased the level of GSH and inhibited TrxR activity, thereby shifting the intracellular balance between ROS generation and antioxidation toward an increase in ROS levels (Figure 2A). Therefore, we next examined whether the lethal effects of APR-246 on ARID1A-deficient cells were due to inhibition of GSH and TrxR. APR-246 treatment dose-dependently decreased the GSH level (presented as the ratio of reduced GSH to its oxidized form, GSH disulfide [GSSG]) in *ARID1A*-KO cells, but not in *ARID1A*-WT cells (Figure 2B). On the other hand, the same concentrations of APR-246 did not affect TrxR activity (including TrxR1, TrxR2, and TrxR3) in *ARID1A*-WT or *ARID1A*-KO cells, while a higher concentration of APR-246 suppressed TrxR activity (Figures 2C and S2A). Notably, the intracellular ROS level, as indicated by intracellular H_2O_2, was increased more in *ARID1A*-KO cells than in *ARID1A*-WT cells (Figure 2D). The increase in ROS level upon APR-246 treatment is consistent with the previous finding that APR-246 binds to and suppresses the functions of antioxidants such as GSH (Bykov et al., 2016). Notably, the ROS level was increased much more in *ARID1A*-KO cells than in *ARID1A*-WT cells, indicating that the level of oxidative stress induced by APR-246 treatment was higher in *ARID1A*-KO cells than in *ARID1A*-WT cells; that is, the balance between ROS generation and antioxidation shifted toward a more oxidized state due to the decreased GSH level in *ARID1A*-KO cells. Indeed, activation of the p38 MAPK and EGFR signaling pathways, which are known to be activated by oxidative stress (Matsuzawa and Ichijo, 2008; Weng et al., 2018), was more evident in *ARID1A*-KO cells treated with ARP-246 (Figure 1L). In addition, an antibody array analysis demonstrated that levels of cyclooxygenase-2 (COX-2), phosphorylated JNK, and phosphorylated HSP27, all of which are induced by oxidative stress, were higher in *ARID1A*-KO cells than in *ARID1A*-WT cells (Figure 2E). Phosphorylation of JNK in response to APR-246 was suppressed by co-treatment with the ROS scavenger N-acetylcysteine (NAC) (Figure 2F). These results indicate that APR-246 induced a state of high oxidative stress in *ARID1A*-KO cells.

The decreased GSH level and increased ROS level after APR-246 treatment were evident only in ARID1A-deficient human ovarian and other cancer cells (Figures 2G, 2H, S2B, and S2C). Stable introduction of the ARID1A cDNA into ARID1A-deficient cancer cells rescued the APR-246-induced decrease in GSH, increase in ROS, and inhibition of cell growth (Figures 2I–2K), indicating that sensitivity to APR-246 was dependent on ARID1A function. In addition, the GSH decrease and ROS increase in APR-246-treated *ARID1A*-KO cells were completely suppressed by co-treatment with the ROS scavenger NAC or the GSH compensator GSH monoethyl ester (GSH-MEE) (Figures 2L and 2M). Consistently, the decrease in cell viability and induction of apoptosis in APR-246-treated *ARID1A*-KO cells were completely abolished by co-treatment with NAC or GSH-MEE (Figures 2N and 2O). Similar results were obtained in two different ARID1A-deficient cancer cell lines (Figures S2D–S2F). These results indicate that inhibition of GSH in ARID1A-deficient cancer cells with APR-246 leads to higher ROS levels by disrupting the balance between ROS generation and antioxidation by GSH, resulting in apoptotic cell death.

MQ derived from APR-246 and PRIMA-1 also binds covalently to cysteine residues in TrxR (Bykov et al., 2016). In fact, *ARID1A*-KO cells and ARID1A-deficient cells were more sensitive to the TrxR inhibitor auranofin than ARID1A-proficient cells (Figures S2G and S2I). The decrease in the GSH level and the increase in the ROS level by auranofin were more evident in ARID1A-deficient cancer cells, as in the case of APR-246 (Figures S2J and S2K). These results indicate that the sensitivity of ARID1A-deficient cancer cells to APR-246 is due mainly to GSH inhibition, as shown in Figures 2B and 2C, but might be also partially due to inhibition of TrxR. MQ also binds to and activates mutant p53, leading to induction of apoptosis (Bykov et al., 2002; Lambert et al., 2009). HCT116 cells express wild-type *TP53*; therefore, it is unlikely that p53 is the target underlying the sensitivity of ARID1A-deficient cells to APR-246. Indeed, depletion of endogenous wild-type p53 did not significantly affect APR-246-induced apoptosis in *ARID1A*-KO cells (Figures S2L and S2N). In addition, treatment with Nutlin3a, an MDM2 inhibitor that stabilizes wild-type p53, increased the p53 level and upregulated the p53 target p21, whereas treatment with PRIMA-1 and APR-246 at concentrations that induced apoptosis did not markedly affect expression of p53 or p21 (Figure S2O). These findings indicate that the sensitivity of ARID1A-deficient cancer cells to APR-246 is not dependent on p53. *NOXA* is a transcriptional target of p53; however, *NOXA* expression induced by APR-246 was not suppressed by p53 depletion in *ARID1A*-KO cells (Figure S2P). Induction of *NOXA* is also caused by JNK signaling pathway activation (Wang et al., 2008). Indeed, *NOXA* expression induced by APR-246 was also suppressed by co-treatment with a JNK inhibitor (Figures S2Q and S2R) or with the ROS scavenger NAC (Figure 2F). Thus, JNK signaling activated by oxidative stress caused *NOXA* upregulation in *ARID1A*-KO cells. However, the decrease in the GSH level and the increase in the ROS level in APR-246-treated

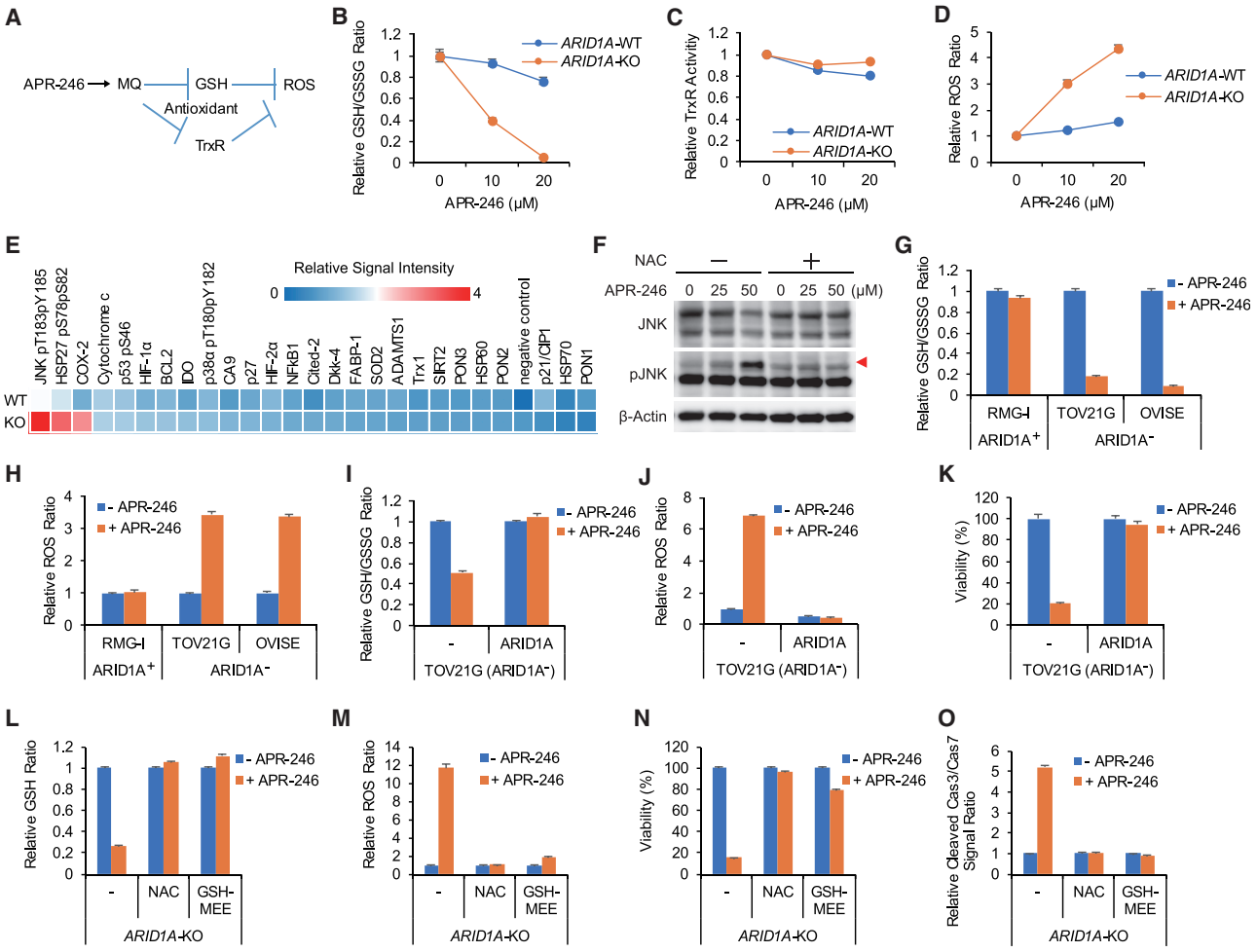

Figure 2. ARID1A-Deficient Cancer Cells Are Vulnerable to GSH Inhibition

(A) Schematic of the candidate targets of APR-246.

(B–D) Relative GSH levels (B), relative TrxR activities (C), and relative ROS levels (D) in *ARID1A*-WT and *ARID1A*-KO HCT116 cells after treatment with APR-246 for 24, 24, and 48 h, respectively.

(E) Heatmap of the ratios of the signal intensities in *ARID1A*-WT and *ARID1A*-KO HCT116 cells treated with 40 μM APR-246 for 24 h relative to the corresponding intensities in untreated cells.

(F) Immunoblotting for JNK, phospho-JNK (pJNK), and β-actin in whole-cell extracts of *ARID1A*-KO HCT116 cells after treatment with 25 or 50 μM APR-246 for 24 h. The red arrowhead indicates the phosphorylated form of JNK.

(G–H) Relative GSH levels (G) and relative ROS levels (H) in RMG-I, TOV21G, and OVISE cells after treatment with 5 μM APR-246 for 16 and 48 h, respectively.

(I–K) Relative GSH levels (I), relative ROS levels (J), and cell viability (K) in ARID1A-deficient TOV21G cancer cells with or without ectopic expression of ARID1A cDNA after treatment with 30 μM APR-246 for 24, 48, and 48 h, respectively.

(L–O) Relative GSH levels (L), relative ROS levels (M), cell viability (N), and levels of apoptosis (O) in *ARID1A*-KO HCT116 cells after treatment with 40 μM APR-246 for 24, 48, 48, and 48 h, respectively, without or with co-treatment with 5 mM NAC or 5 mM GSH-MEE.

Data in (B–D, and G–O) are expressed as the mean ± SD. See also Figure S2.

ARID1A-KO cells were not suppressed by co-treatment with the JNK inhibitor or by NOXA depletion (Figures S2S–S2W). Therefore, activation of the JNK signaling pathway and the resulting increase in *NOXA* expression seem to be secondary effects of oxidative stress and not the mediators causing lethality.

GCLC Is a Promising Synthetic Lethal Target in ARID1A-Deficient Cancers

GSH is synthesized from cysteine, glutamate, and glycine via the actions of multiple metabolic factors (Figure 3A). To identify therapeutic targets against ARID1A-deficient cancers in the GSH metabolic pathway, GSH metabolic pathway genes were screened for a synthetic lethal partnership with *ARID1A*. Subsequent analyses revealed that knockdown of GCLC, GSS, and SLC7A11 significantly and specifically suppressed the growth of ARID1A-deficient cancer cells, in association with a decrease in the GSH level and an increase in the ROS level (Figures 3B–3D). On the other hand, even simultaneous knockdown of functional paralog gene products such as GLS and GLS2, SLC1A4 and SLC1A5, and IDH1 and IDH2, which are considered to play redundant roles, did not affect the growth of ARID1A-deficient cancer cells (Figure 3B). Furthermore, knockdown of

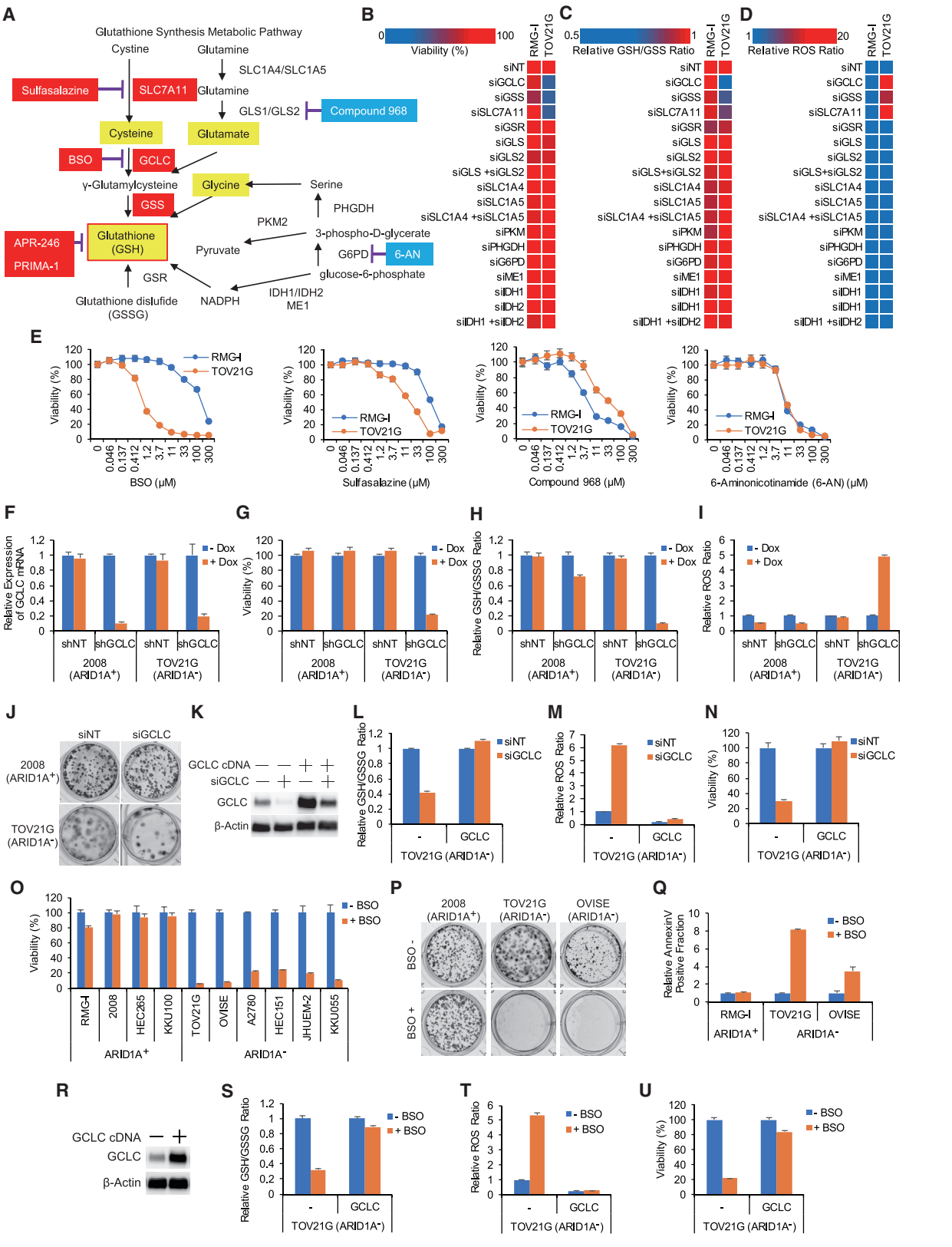

(legend on next page)

anti-ROS gene products belonging to the TrxR and superoxide dismutase families did not markedly affect cell growth, the GSH level, or the ROS level, even when gene products from multiple families were simultaneously knocked down (Figures S3A–S3C). Next, known inhibitors of GSH metabolic factors were screened for their selectivity for ARID1A-deficient cancers. ARID1A-deficient TOV21G ovarian cancer cells were more sensitive than ARID1A-proficient RMG-I ovarian cancer cells to the GCLC inhibitor buthionine sulfoximine (BSO) and the SLC7A11 inhibitor sulfasalazine, but not to the GLS inhibitor compound 968 or the G6PD inhibitor 6-aminonicotinamide (Figure 3E), consistent with the knockdown experiments. Similar results were obtained using *ARID1A*-KO and *ARID1A*-WT cells (Figure S3D). Knockdown of GCLC, GSS, or SLC7A11 inhibited the growth of ARID1A-deficient OVISE ovarian cancer cells, in association with a decrease in the GSH level and an increase in the ROS level (Figures S3E–S3J). The decrease in GSH level, the increase in ROS level, and the inhibition of cell growth caused by knockdown of GCLC and SLC7A11 in ARID1A-deficient TOV21G cells were rescued by stable expression of the ARID1A cDNA (Figures S3K–S3O), confirming that ARID1A deficiency is responsible for the sensitivity to depletion of those genes.

Among the three GSH synthesis pathway enzymes listed above, we focused on GCLC because it is a rate-limiting enzyme (i.e., possibly a druggable target) in GSH synthesis and its transient knockdown markedly inhibited the growth of ARID1A-deficient cancer cells (Figure S3H). In fact, stable short hairpin RNA (shRNA)-mediated knockdown of GCLC induced by treatment with doxycycline (Dox) selectively inhibited the growth of ARID1A-deficient cancer cells (Figures 3F–3G). GSH and ROS levels were significantly decreased and increased, respectively, in ARID1A-deficient cancer cells but not ARID1A-proficient cells (Figures 3H and 3I). Similar results were obtained using *ARID1A*-KO and *ARID1A*-WT cells (Figures S3P–S3S). The lethality of GCLC depletion in ARID1A-deficient cancer cells was validated by measuring cell survival in colony formation assays (Figures 3J, S3T, and S3U). Ectopic expression of GCLC abrogated the decrease in the GSH level upon knockdown of GCLC in ARID1A-deficient cell lines and *ARID1A*-KO cells (Figures 3K, 3L, S3V, and S3W). In addition, ectopic GCLC expression abrogated ROS production and subsequent cell death upon GCLC knockdown (Figures 3M, 3N, S3X, and S3Y). Taken together, these data indicate that GCLC is a synthetic lethal target in ARID1A-deficient cancer cells.

To determine whether GCLC is a druggable target, we examined the sensitivities of four ARID1A-proficient and six ARID1A-deficient cancer cell lines to the GCLC inhibitor BSO. ARID1A-deficient cancer cell lines were selectively sensitive to BSO (Figures 3O and S4A). Colony formation assays demonstrated that BSO selectively reduced survival and increased apoptosis of ARID1A-deficient cancer cell lines and *ARID1A*-KO cells (Figures 3P, 3Q, and S4B–S4E). BSO treatment decreased the GSH level, which was associated with increased ROS levels and *NOXA* expression, and this effect was more prominent in ARID1A-deficient cancer cells (Figures S4F–S4J). Stable expression of ARID1A abrogated the BSO-induced decrease in GSH, increase in ROS, and inhibition of cell growth of ARID1A-deficient cancer cells (Figures S4K–S4M), indicating that the observed responses to BSO are dependent on ARID1A. The BSO-induced decrease in GSH in ARID1A-deficient cancer cells was attenuated by the GSH compensator GSH-MEE, but not by the ROS scavenger NAC (Figure S4N). The APR-246-induced decrease in GSH in ARID1A-deficient cancer cells was suppressed by both GSH-MEE and NAC (Figures 2L and S2D), consistent with the fact that NAC inhibits ROS and APR-246 activity by forming adducts (Lambert et al., 2009). Both GSH-MEE and NAC abrogated the BSO-induced increase in ROS and inhibition of cell growth (Figures S4O and S4P). These results indicate that even when GSH production is decreased by BSO treatment, NAC and GSH-MEE restore cell viability by scavenging excessive ROS and compensating for GSH, respectively. Ectopic expression of GCLC suppressed all the effects of BSO and APR-246 in ARID1A-deficient cancer cells, including the decrease in GSH, the increase in ROS, and the inhibition of cell growth (Figures 3R–3U, S4Q, and S4S). These results strongly suggest that GCLC is a druggable target in ARID1A-deficient cancer cells.

Vulnerability of ARID1A-Deficient Cancer Cells to GSH Inhibition Is Caused by Decreased GSH Synthesis due to Impaired *SLC7A11* Expression

ARID1A-deficient cancer cells were sensitive to GSH inhibition compared with ARID1A-proficient cells. We therefore hypothesized that ARID1A regulates transcription of genes encoding components of the GSH synthesis pathway. To investigate this, a genome-wide expression analysis of a panel of ARID1A-proficient

Figure 3. GCLC Is a Promising Synthetic Lethal Target in ARID1A-Deficient Cancers

(A) Schematic of molecules involved in the GSH metabolic pathway and inhibitors of their products.

(B–D) Heatmaps of cell viability (B), relative GSH levels (C), and relative ROS levels (D) in ARID1A-proficient RMG-I cells and ARID1A-deficient TOV21G cells at 5, 3, and 3 days, respectively, after knockdown of GSH pathway genes.

(E) Cell viability of ARID1A-proficient RMG-I cells and ARID1A-deficient TOV21G cells after treatment with BSO, sulfasalazine, compound 968, or 6-aminonicotinamide for 3 days.

(F–I) Relative GCLC mRNA levels (F), cell viability (G), relative GSH levels (H), and relative ROS levels (I) in ARID1A-proficient 2008 cells and ARID1A-deficient TOV21G cells at 3 days after shRNA-mediated knockdown of GCLC by treatment with 0.5 μg/mL doxycycline (Dox).

(J) Colony formation of 2008 and TOV21G cells at 14 days after knockdown of GCLC genes.

(K–N) Immunoblotting for GCLC and β-actin in whole-cell extracts (K), relative GSH levels (L; 3 days), relative ROS levels (M; 3 days), and cell viability (N; 7 days) in parental TOV21G cells and TOV21G cells stably expressing GCLC after knockdown of GCLC.

(O) Cell viability of cancer cell lines after treatment with 33 μM BSO for 3 days.

(P) Colony formation of 2008, TOV21G, and OVISE cancer cells at 14 days after treatment with 10 μM BSO.

(Q) Detection of Annexin V-positive apoptotic cells in 2008, TOV21G, and OVISE cells after treatment with 200 μM BSO for 72 h.

(R–U) Immunoblotting for GCLC and β-actin in whole-cell extracts (R), relative GSH levels (S; 1 day), relative ROS levels (T; 1 day), and cell viability (U; 2 days) in parental TOV21G cells and TOV21G cells stably expressing GCLC after treatment with 100 μM BSO.

Data in (E–I, L–O, Q, and S–U) are expressed as the mean ± SD. See also Figures S3 and S4.

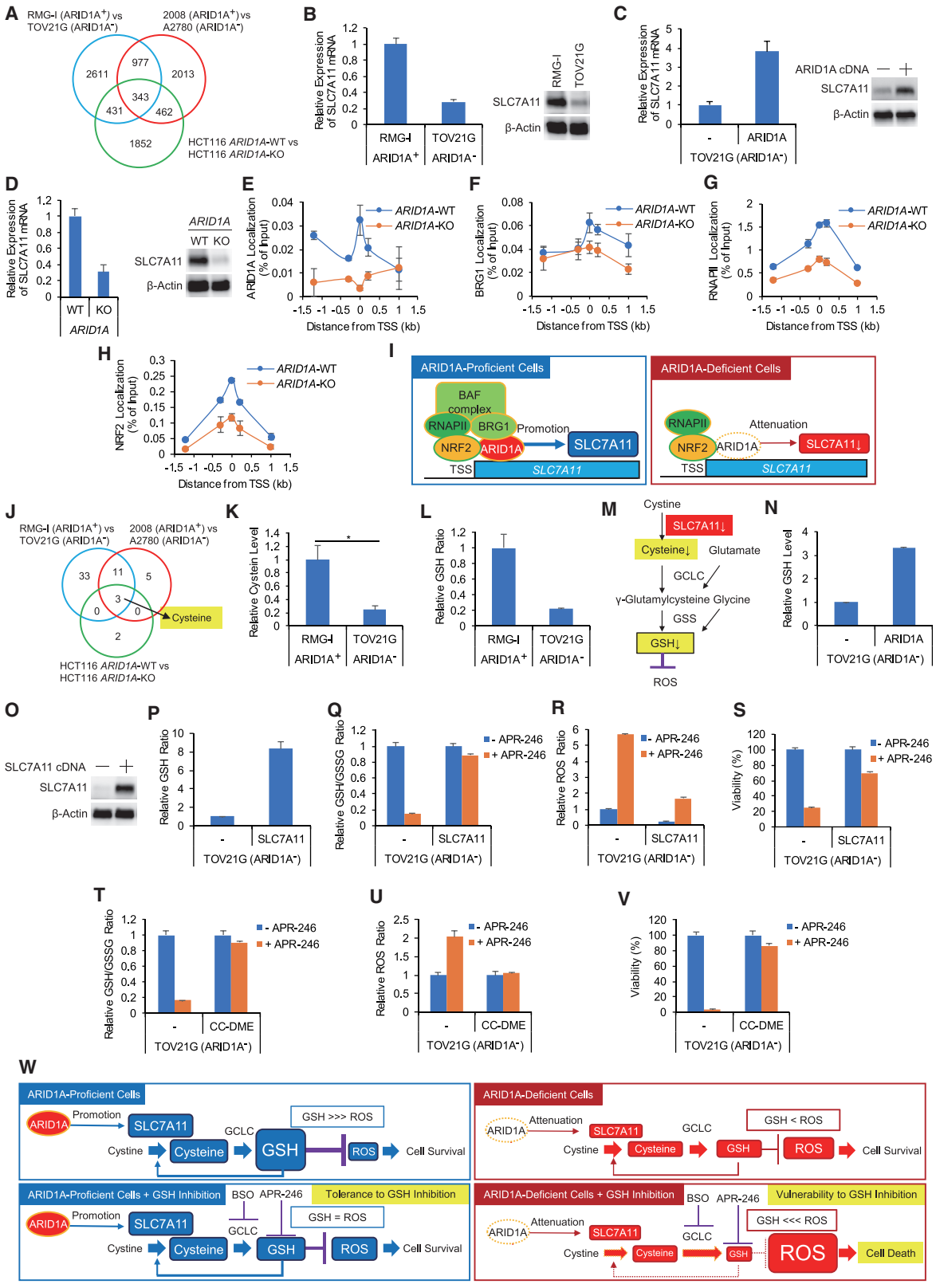

(legend on next page)

and ARID1A-deficient cancer cells was performed. In total, 343 genes whose expression levels were consistently more than 1.5-fold lower in ARID1A-deficient cancer cells were identified (Figure 4A). Notably, this gene set included only one GSH metabolic pathway gene, *SLC7A11*. Expression of SLC7A11 mRNA and protein was lower in ARID1A-deficient cancer cells than in ARID1A-proficient cancer cells (Figures 4B and S5A–S5C). Stable expression of ARID1A in ARID1A-deficient cancer cells restored expression of SLC7A11 mRNA and protein (Figure 4C). In addition, knockout of *ARID1A* decreased expression of SLC7A11 (Figure 4D). To determine the mechanism underlying the impaired induction of *SLC7A11* in *ARID1A*-KO cells, the involvement of ARID1A in the transcriptional upregulation of *SLC7A11* was investigated. A chromatin immunoprecipitation (ChIP) assay revealed that ARID1A localized at the transcription start site (TSS) of *SLC7A11* in *ARID1A*-WT cells (Figure 4E). Likewise, BRG1, the catalytic subunit of the SWI/SNF chromatin-remodeling complex (the BAF complex) that contains ARID1A, localized at the TSS of *SLC7A11* in *ARID1A*-WT cells (Figure 4F). Localization of ARID1A and BRG1 at the TSS was impaired in *ARID1A*-KO cells (Figures 4E and 4F). Localization of RNA polymerase II (RNAPII) at the TSS was also markedly impaired in *ARID1A*-KO cells (Figure 4G). Localization of NRF2, a transcription factor regulating *SLC7A11* expression (Gorrini et al., 2013), at the TSS was also markedly impaired in *ARID1A*-KO cells (Figure 4H), whereas expression of NRF2 itself was not affected by knockout of *ARID1A* (Figure S5D). Ectopic expression of NRF2 in *ARID1A*-KO cells restored expression of SLC7A11 mRNA and protein (Figures S5D and S5E), restored the APR-246-induced decrease in growth and survival, and abrogated the APR-246-induced decrease in GSH and increase in ROS (Figures S5F and S5I). These results strongly suggest that ARID1A promotes, but is not essential for, NRF2-mediated transcriptional expression of *SLC7A11* through chromatin remodeling by the BAF complex. In other words, ARID1A deficiency causes attenuation of *SLC7A11* expression (Figure 4I).

SLC7A11 encodes a subunit of the cystine/glutamate transporter XCT. Cystine is taken up into cells through the XCT transporter and is then metabolized into two molecules of cysteine, which is essential for GSH synthesis. To investigate the effects of downregulation of *SLC7A11* caused by ARID1A deficiency, we screened metabolites whose levels were decreased in the three pairs of ARID1A-proficient and ARID1A-deficient cells using gas chromatography/mass spectrometry, which is able to detect 475 metabolites (including cysteine, glutamate, and glycine, but not GSH) (Figure 4J). Cysteine was identified as a metabolite that was more than 2-fold lower in ARID1A-deficient cells than in ARID1A-proficient cells (Figures 4J–K and S5J), suggesting that *SLC7A11* downregulation caused a decrease in intracellular cysteine levels due to impaired uptake of cystine into cells. Consistent with the decreased level of cysteine in ARID1A-deficient cells, the basal GSH level was lower in ARID1A-deficient cells than in ARID1A-proficient cells (Figures 4L, 4M, S5K, and S5L). Reflecting the increased GSH level, the ROS level was higher in ARID1A-deficient cells than in ARID1A-proficient cells (Figures S5M–S5O). As shown in Figure 4C, stable expression of ARID1A in ARID1A-deficient cancer cells increased SLC7A11 expression, which was associated with an increase in the GSH level and a decrease in the ROS levels (Figures 4N and S5P). These results indicate that ARID1A affects the balance between the basal levels of GSH and ROS through expression of *SLC7A11*. Consistently, forced expression of SLC7A11 in ARID1A-deficient cancer cells increased the basal GSH levels, which was associated with decreased basal ROS levels (Figures 4O, 4P, and S5Q). Similar results were obtained by stable expression of GCLC in ARID1A-deficient cancer cells (Figures S5R and S5S). Overexpression of SLC7A11 abrogated the APR-246- and BSO-induced decreases in the GSH level and increases in the ROS level, and restored the viability of ARID1A-deficient cancer cells (Figures 4Q–4S and S5T–S5V).

The decrease in GSH, increase in ROS, and decrease in viability in APR-246-treated ARID1A-deficient cancer cells were completely suppressed by co-treatment with the cystine compensator cystine dimethyl ester (CC-DME), a cell-permeable version of cystine (Steinherz et al., 1982) (Figures 4T–4V). These data

Figure 4. Vulnerability of ARID1A-Deficient Cancer Cells to GSH Inhibition Is Caused by Decreased GSH Synthesis due to Impaired *SLC7A11* Expression

(A) A Venn diagram showing the numbers of significantly downregulated (fold change < −1.5) genes in ARID1A-deficient cells compared with ARID1A-proficient cells.
(B) Relative expression of SLC7A11 mRNA (left) and protein (right) in ARID1A-proficient RMG-I cells and ARID1A-deficient TOV21G cells.
(C) Relative expression of SLC7A11 mRNA (left) and protein (right) in parental TOV21G cells and TOV21G cells stably expressing ARID1A.
(D) Relative expression of SLC7A11 mRNA (left) and protein (right) in *ARID1A*-WT and *ARID1A*-KO HCT116 cells.
(E–H) ChIP analysis of the localization of ARID1A (E), BRG1 (F), RNAPII (G), and NRF2 (H) around the TSS of *SLC7A11* in *ARID1A*-WT and *ARID1A*-KO HCT116 cells.
(I) Schematic of the mechanism underlying regulation of *SLC7A11* expression by ARID1A.
(J) A Venn diagram showing metabolites downregulated (fold change < −2) in ARID1A-deficient cells compared with ARID1A-proficient cells.
(K) Basal cysteine levels in ARID1A-proficient RMG-I cells and ARID1A-deficient TOV21G cells. Data are expressed as the mean ± SEM (n = 3). *p < 0.05; two-tailed t test.
(L) Basal GSH levels in ARID1A-proficient RMG-I cells and ARID1A-deficient TOV21G cells.
(M) Schematic of the GSH synthesis pathway.
(N) Basal GSH levels in parental TOV21G cells and TOV21G cells stably expressing ARID1A.
(O and P) Immunoblotting for SLC7A11 and β-actin (O) and the basal GSH level (P) in parental TOV21G cells and TOV21G cells stably expressing SLC7A11.
(Q–S) Relative GSH levels (Q), relative ROS levels (R), and cell viability (S) in parental TOV21G cells and TOV21G cells stably expressing SLC7A11 after treatment with 20 μM APR-246 for 24 h.
(T–V) Relative GSH levels (T), relative ROS levels (U), and cell viability (V) in ARID1A-deficient TOV21G cells after treatment with 30 μM APR-246 for 24 and 48 h, respectively, without or with co-treatment with 100 μM CC-DME.
(W) Schematic model explaining the vulnerability of ARID1A-deficient cancers to inhibition of GSH metabolism. The signs of (in)equality indicate the balance between GSH activity and ROS.
Data in (B–H, L, N, and P–V) are expressed as the mean ± SD. See also Figure S5.

indicate that a cysteine shortage due to impaired *SLC7A11* expression in ARID1A-deficient cancer cells is the cause of their vulnerability to inhibition of the GSH metabolic pathway. Collectively, these results lead us to propose the following mechanism (Figures 4I and 4W). ARID1A facilitates recruitment of the SWI/SNF chromatin-remodeling complex to the TSS of *SLC7A11*, and the resultant remodeling initiates the transcription of *SLC7A11* by NRF2 and RNAPII. Enhanced cystine uptake by SLC7A11 upregulates GSH synthesis via GCLC, maintaining the homeostatic balance between GSH and ROS and making cells tolerant of GSH inhibition. However, in the absence of ARID1A, impaired recruitment of the SWI/SNF chromatin-remodeling complex to the TSS of *SLC7A11* attenuates recruitment of NRF2 and RNAPII to this site, resulting in impaired transcription of *SLC7A11*. The resultant decrease in cystine uptake impairs GSH synthesis. In addition, impairment of the feedback function of GSH to produce cysteine from cystine would further decrease the intracellular level of cysteine and eventually lead to shortage of GSH due to perturbed homeostasis of the antioxidant system. The decrease in the basal GSH level makes ARID1A-deficient cancer cells vulnerable to inhibition of the GSH metabolic pathway.

Clinical Relevance of GSH-Targeting Therapy for ARID1A-Deficient Cancers

To further address the clinical relevance of this hypothesis, we examined expression of ARID1A and SLC7A11 by immunohistochemical (IHC) staining of tumor specimens surgically obtained from 11 ovarian cancer patients (Figure S6A). All four *ARID1A* wild-type specimens examined showed high expression of both ARID1A and SLC7A11 (Figure 5A), while all four of the *ARID1A*-mutated specimens lacking ARID1A expression showed low levels of SLC7A11 expression (Figure 5B). The remaining three *ARID1A*-mutated specimens, which retained ARID1A expression, also retained SLC7A11 expression (Figures S6A and S6B). Taken together, reduced/absent ARID1A expression due to *ARID1A* gene mutations correlated with decreased SLC7A11 expression in clinically obtained tumor specimens.

Patient-derived cancer cells (PDCs) often serve as a tool to obtain proof-of-concept for cancer therapy. Thus, PDCs from four other ovarian cancer patients, of which three cases lacked ARID1A, whereas the remaining case retained ARID1A expression, were cultured (Figure 5C). Consistent with the results obtained using cancer cell lines, ARID1A-deficient PDCs were more sensitive to APR-246 and BSO than ARID1A-positive PDCs (Figures 5D and S6C). In addition, expression of SLC7A11 mRNA and protein in ARID1A-deficient PDCs was low, which is in agreement with the observations in tumor specimens described above (Figures 5E–5F). Basal GSH levels were lower in ARID1A-deficient PDCs than in ARID1A-proficient PDCs (Figure 5G), while basal ROS levels were higher (Figure S6D). APR-246 treatment decreased the GSH levels in ARID1A-deficient PDCs and increased the levels of ROS and apoptosis (Figures 5H–5J and S6E).

Next, APR-246 was tested for its ability to suppress the growth of OCCC tumor xenografts *in vivo*. After tumor formation, mice were treated with APR-246 or vehicle. APR-246 treatment significantly suppressed the growth of ARID1A-deficient TOV21G OCCC xenografts, but not that of ARID1A-proficient RMG-I OCCC xenografts (Figures 6A and 6B). Consistently, tumor weight was reduced by APR-246 only in TOV21G xenografts (Figures 6C and 6D). Treatment of mice with APR-246 did not cause significant loss of body weight, indicating that APR-246 has minimal adverse effects (Figure S6F), consistent with the results of a phase I clinical trial (Lehmann et al., 2012). Notably, the GSH level in TOV21G xenograft cells decreased after treatment with APR-246 (Figure 6E). In addition, APR-246 increased the level of the oxidative stress marker 8-hydroxy-2′-deoxyguanosine (8-OHdG) markedly, indicating that APR-246 increased the ROS levels in TOV21G xenografts *in vivo* (Figures 6F and 6G). In addition, APR-246 treatment markedly increased expression of the apoptotic markers NOXA, cleaved PARP, and cleaved caspase-3, and decreased expression of the cell proliferation marker Ki67, indicating that apoptosis was also induced by treatment with APR-246 *in vivo* (Figures 6F, 6H, and 6G). Consistently, APR-246 analog PRIMA-1 treatment also significantly suppressed the growth of xenografts in ARID1A-deficient OVISE OCCC cells, again without causing significant weight loss (Figures S6G and S6H). In addition, treatment with the GCLC inhibitor BSO markedly suppressed xenograft growth, resulting in reduced tumor weight without loss of body weight (Figures S6I–S6K). The present results obtained using drugs inhibiting GSH function via different mechanisms demonstrate the utility of targeting GCLC in ARID1A-deficient OCCCs.

To further validate GCLC as a therapeutic target, the effects of GCLC depletion were assessed in an ARID1A-deficient OCCC tumor xenograft model. TOV21G OCCC cells carrying non-targeting (shNT) or GCLC-targeting (shGCLC) shRNAs were injected into mice. *GCLC* expression in TOV21G-shGCLC cells was conditionally reduced by Dox (Figure 3F). When mice were fed with Dox to induce GCLC depletion after tumor formation, the growth of TOV21G-shGCLC xenografts was suppressed significantly, resulting in reduced tumor weight, whereas the growth of TOV21G-shNT xenografts was not affected (Figures 6L–6O). Knockdown of GCLC in TOV21G-shGCLC xenografts, but not in TOV21G-shNT xenografts, was confirmed in tumors from mice treated with Dox (Figures S6L and S6M). The GSH level in TOV21G-shGCLC xenograft cells decreased *in vivo* after treatment with Dox (Figure 6P). Similar results were also obtained when mice were fed Dox immediately after inoculation of cells (before tumor formation) (Figures S6N–S6R). As with APR-246 treatment of TOV21G xenografts, Dox-mediated knockdown of GCLC in TOV21G-shGCLC xenografts markedly increased the level of the oxidative stress marker 8-OHdG, increased the levels of the apoptosis markers NOXA, cleaved caspase-3, and cleaved PARP, and decreased the level of the cell proliferation marker, Ki67. These results indicate that ROS levels and apoptosis were increased by inhibition of GCLC *in vivo* (Figure S6S). Taken together, we conclude that GCLC is a therapeutic target in ARID1A-deficient OCCCs.

DISCUSSION

This study identified a druggable and addictive antioxidant-related molecule for ARID1A-deficient cancers. We found that ARID1A-deficient cancer cells were sensitive to APR-246 and PRIMA-1, which covalently bind to cysteine residues in multiple polypeptides (Bykov et al., 2016). PRIMA-1 was originally developed as a compound that reactivates mutant p53 (Chipuk et al., 2003). However, PRIMA-1 and its analog APR-246 have p53-independent anti-cancer activities; specifically, these compounds

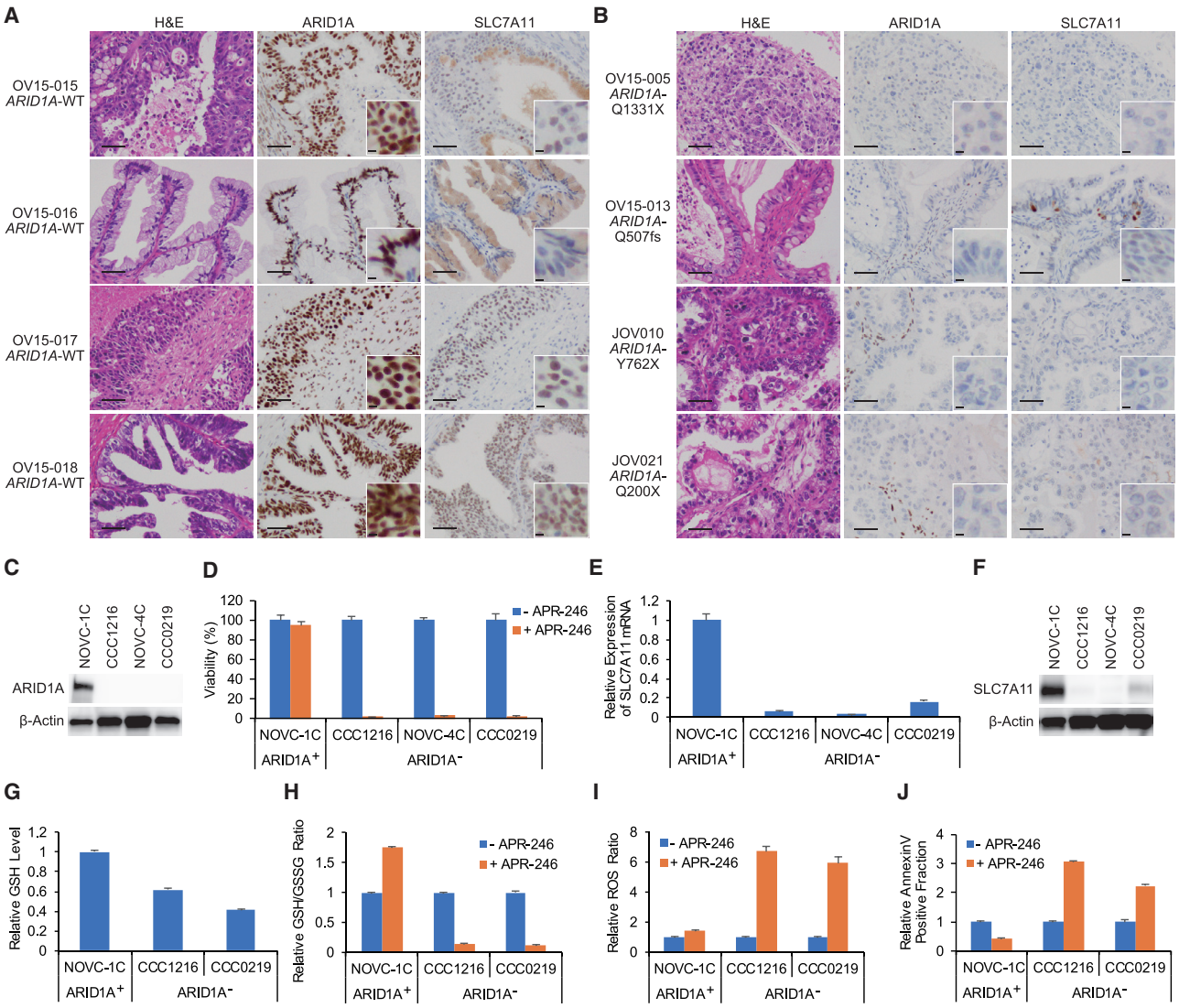

Figure 5. Clinical Relevance of GSH-Targeting Therapy for ARID1A-Deficient Cancers

(A and B) Immunohistochemical staining for ARID1A and SLC7A11 in ovarian cancer specimens with wild-type (A) or mutant (B) *ARID1A*. Scale bar, 50 μm.

(C) Immunoblotting for ARID1A and β-actin in whole-cell extracts of ovarian PDCs.

(D) Cell viability of ovarian PDCs after treatment with 33 μM APR-246 for 6 days.

(E and F) Relative expression of SLC7A11 mRNA (E) and protein (F) in ovarian PDCs.

(G) Basal GSH levels in ovarian PDCs.

(H and I) Relative GSH levels (H) and relative ROS levels (I) in ovarian PDCs after treatment with 50 μM APR-246 for 24 h.

(J) Detection of Annexin V-positive apoptotic cells in ovarian PDCs after treatment with 40 μM APR-246 for 48 h.

Data in (D, E, and G–J) are expressed as the mean ± SD. See also Figure S6.

bind to and inhibit the antioxidant factors GSH and TrxR (Grellety et al., 2015; Tessoulin et al., 2014). In this study, p53 deficiency did not affect the sensitivity of ARID1A-deficient cells to APR-246. Our findings indicate that GSH is a major target of APR-246 and underlies the high sensitivity of ARID1A-deficient cancer cells to this compound. This idea is supported by the finding that GSH complementation abrogated APR-246 sensitivity and that ARID1A-deficient cancer cells were highly sensitive to BSO, an inhibitor of GCLC, which is a rate-limiting enzyme for GSH synthesis. Antioxidant defense systems are considered promising targets for cancer therapy (Gorrini et al., 2013; Harris et al., 2015). Here, GSH inhibition caused synthetic lethality in ARID1A-deficient cancer cells, which have a low level of SLC7A11 expression. This is consistent with a report showing that combined treatment with inhibitors of GSH and SLC7A11 synergistically enhances cell death (Harris et al., 2015). Therefore, the present study provides a strong evidence that the sensitivity of cancer cells to inhibition of the antioxidant GSH metabolic system by targeting GCLC is defined by ARID1A deficiency, which is a genetic aberration commonly observed in a variety of human cancers.

We showed that ARID1A-deficient cancer cells are sensitive to the TrxR inhibitor auranofin in addition to APR-246, but not

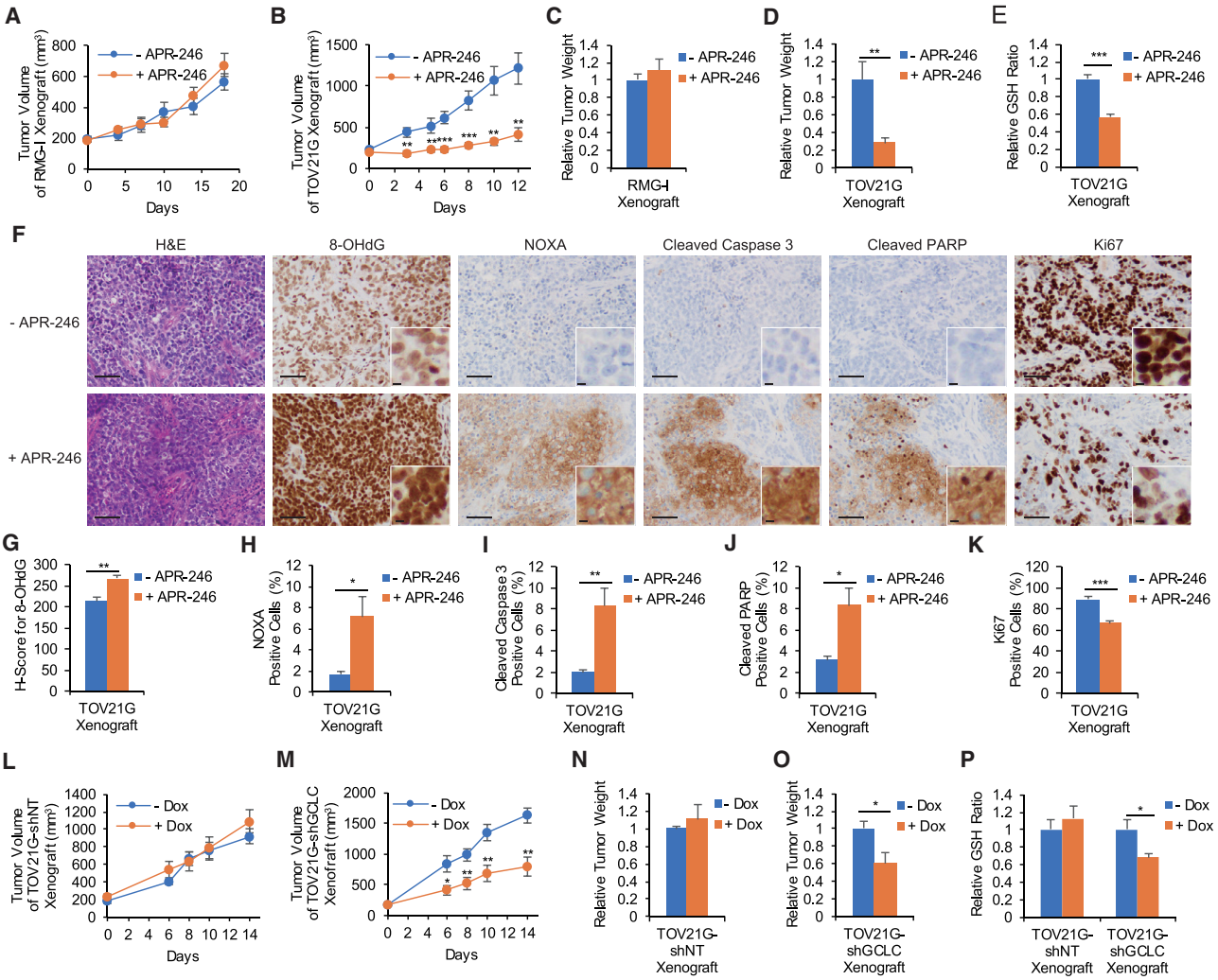

Figure 6. Anti-tumor Effect of GSH-Targeting Therapy for ARID1A-Deficient Cancers

(A–D) Tumor volume (A and B) and relative tumor weights (C and D) of xenografts derived from ARID1A-proficient RMG-I (A and C) or ARID1A-deficient TOV21G (B and D) cells in mice treated with 50 mg/kg APR-246 (n = 6).

(E) Relative GSH ratio in xenografts derived from ARID1A-deficient TOV21G cells in mice treated with 50 mg/kg APR-246 (n = 6).

(F) Immunohistochemical (IHC) staining for 8-OHdG, NOXA, cleaved caspase-3, cleaved PARP, and Ki67 in xenografts derived from ARID1A-deficient TOV21G cells in mice treated with 50 mg/kg APR-246. Scale bar, 50 μm.

(G) Histological score (H-score) of IHC staining for 8-OHdG in xenografts derived from ARID1A-deficient TOV21G cells in mice treated with 50 mg/kg APR-246 (n = 6).

(H–K) Percentage of cells staining positive for NOXA (H), cleaved caspase-3 (I), cleaved PARP (J), and Ki67 (K) in tumor of xenografts derived from ARID1A-deficient TOV21G cells in mice treated with 50 mg/kg APR-246 (n = 6).

(L–O) Tumor volume (L and M) and relative tumor weight (N and O) of xenografts derived from TOV21G-shNT (L and N) and TOV21G-shGCLC (M and O) cells in mice treated without or with doxycycline (Dox). After tumor formation, mice were fed a diet with or without Dox (n = 6).

(P) Relative GSH levels in tumor of xenografts derived from TOV21G-shNT and TOV21G-shGCLC cells in mice treated without or with Dox (n = 6).

Data in (A–E and G–P) are expressed as the mean ± SEM. *p < 0.05, **p < 0.01, ***p < 0.001; two-tailed t test. See also Figure S6.

to the depletion of TrxR. TrxR regenerates an antioxidant thioredoxin by using NADPH oxidase (Gorrini et al., 2013). APR-246 inhibits the activity of TrxR and transforms the activity as a reductase of TrxR to an NADPH oxidase, which is an inducer of ROS (Peng et al., 2013), indicating that direct inhibition, but not depletion, of TrxR might contribute to sensitivity of ARID1A-deficient cancer cells. GSH and thioredoxin redundantly defend against oxidative stress, and a synergistic antitumor effect of combined GSH and TrxR inhibition has been reported (Harris et al., 2015). Thus, simultaneous inhibition of GSH and TrxR by dual inhibitors such as APR-246 or combined treatment with GSH and TrxR inhibitors might be a potent therapeutic strategy worth investigating further.

The vulnerability of the GSH metabolic pathway in ARID1A-deficient cancer cells is likely augmented by a reduced DNA damage response associated with ARID1A deficiency. ARID1A functions in DNA double-strand break (DSB) repair following ionizing irradiation (Shen et al., 2015). Accumulation of DSBs due to perturbed DSB repair would increase apoptosis. Activation of JNK signaling, which is caused by oxidative and DNA damage

stress (Zeke et al., 2016), leads to upregulation of the pro-apoptotic factor NOXA. Thus, the enhanced apoptosis observed in ARID1A-deficient cancer cells upon inhibition of the GSH metabolic pathway is explained by the following model. Depletion of GSH leads to excessive ROS levels and, consequently, DSBs. Insufficient DNA damage responses in ARID1A-deficient cancer cells lead to a further increase in ROS-induced DSBs, which enhances the effect of GSH metabolic pathway inhibition and JNK-mediated NOXA expression, ultimately leading to apoptosis. Therefore, GCLC is a key factor that increases the vulnerability of ARID1A-deficient cancer cells to GSH inhibition via disruption of both the antioxidant system and the DNA damage response.

Mutation rates of *ARID1A* are high in multiple cancer types (Lawrence et al., 2014). The majority, but not all, of *ARID1A*-mutated tumors show loss of ARID1A protein expression (Jones et al., 2010; Wiegand et al., 2010; Wu and Roberts, 2013). Selective sensitivity to APR-246 according to ARID1A deficiency was observed in a variety of cancer cell lines established a long time ago and in recently established ovarian PDCs. Based on results reported here, we propose that *ARID1A*-mutated tumors without ARID1A protein expression, but not those retaining ARID1A expression, will respond well to GSH/GCLC-targeted therapy, since they have low GSH levels due to low SLC7A11 expression. Immunohistochemical assessment of ARID1A protein will be a useful diagnostic tool for selecting patients suitable for GCLC-targeted therapy. APR-246 inhibits multiple thiol-containing proteins in addition to GSH, suggesting its limited utility as well as the possibility of off-target toxicity. However, APR-246 treatment suppressed the growth of xenografts derived from ARID1A-deficient OCCC cells significantly without causing marked body weight loss in mice. A human clinical trial of APR-246 reported a low rate of side effects (Lehmann et al., 2012). The majority of OCCC is ARID1A deficient and *TP53* proficient, while high-grade serous ovarian cancer (HGSOC), another major histological type of ovarian cancer, shows the opposite genotype (Kadoch et al., 2013). Notably in this regard, APR-246 is now being tested as a p53 activator in a phase Ib/II clinical trial for HGSOC (Bykov et al., 2016). APR-246, and other drugs targeting GSH metabolism, is also a candidate drug for OCCCs without ARID1A expression.

Drugs targeting a deficiency in chromatin regulators are expected to show great promise as anti-cancer therapeutics. Previously, we proposed a strategy to target chromatin-regulating proteins that functionally complements the role of a chromatin regulator deficient in cancer (Ogiwara et al., 2016; Oike et al., 2013). In this study, we propose another therapeutic approach for cancers with a deficiency in a chromatin regulator, ARID1A; this approach focuses on GSH metabolism. This strategy must be validated in patients with ARID1A-deficient cancer, especially those with ovarian cancer. In addition, the present findings will also help to elucidate relationships between the metabolic properties of cancer cells and the efficacy of anti-cancer therapeutics.

STAR★METHODS

Detailed methods are provided in the online version of this paper and include the following:

- KEY RESOURCES TABLE
- CONTACTS FOR REAGENT AND RESOURCE SHARING
- EXPERIMENTAL MODEL AND SUBJECT DETAILS
  - Establishment of Ovarian Cancer PDCs
  - Mouse Xenograft Model
  - Cell Lines
  - Generation of shRNA- and cDNA-Expressing Lentiviruses and Virus-Infected Cells
- METHOD DETAILS
  - Drug Library Screen
  - Cell Viability Assay
  - Colony Formation Assay
  - Annexin V/Propidium Iodide (PI) Staining Assay
  - Detection of, GSH, ROS and Cleaved Caspase-3/7 in Cell Lines
  - Detection of GSH in Tumor Samples
  - Detection of TrxR Activity
  - Cell Stress Profiling by Antibody Array
  - Transcriptomic Profiling by Microarray
  - Quantitation of mRNA
  - Immunoblot Analysis
  - ChIP Assay
  - Metabolome Analysis
  - Targeted and Whole-Exome Sequencing
  - Immunohistochemistry
- QUANTIFICATION AND STATISTICAL ANALYSIS
  - Statistical Analysis
- DATA AND SOFTWARE AVAILABILITY

SUPPLEMENTAL INFORMATION

Supplemental Information includes six figures and one table and can be found with this article online at https://doi.org/10.1016/j.ccell.2018.12.009.

ACKNOWLEDGMENTS

We thank Yoko Shimada, Hitoshi Ichikawa, and Naoto Tsuchiya for technical assistance and helpful comments. We also thank the Scientific Support Programs for Cancer Research Grants-in-Aid for Scientific Research on Innovative Areas of the Ministry of Education, Culture, Sports, Science and Technology for providing the SCADS Inhibitor Kit and performing genotyping analysis of cell lines. This study was supported in part by Grants-in-Aid for Scientific Research on Innovative Areas from the Ministry of Education, Culture, Sports, Science, and Technology of Japan (JP22131006); Grants-in-Aid for Young Scientists (B) and Scientific Research (C) KAKENHI from the Japan Society for the Promotion of Science (JP26830122, JP17K11310); and Practical Research for Innovative Cancer Control from the Japan Agency for Medical Research and Development (JP17ck0106168, JP17ck0106374, and JP18ck0106374). The National Cancer Center Biobank is supported by the National Cancer Center Research and Development Fund. Metabolome analysis was supported in part by research funds from the Yamagata Prefectural Government and the city of Tsuruoka.

AUTHOR CONTRIBUTIONS

Conceptualization: H.O.; Methodology: H.O., K.T., M.S., H.M., H.Y.; Formal Analysis and Investigation: H.O., K.T., M.S., T. Kuroda, A.M., H.Y.; Resources: H.O., K.T., M.S., F.C., H.S., R.W., H.Y., T. Kato, A.O.; Writing – Original Draft Preparation: H.O.; Writing – Review and Editing: H.O., T. Kohno; Supervision: H.O., T. Kohno; Project Administration: H.O.; Funding Acquisition: H.O., T. Kato, T. Kohno.

DECLARATIONS OF INTEREST

The authors have no competing interests to declare.

Received: August 6, 2018
Revised: October 29, 2018
Accepted: December 21, 2018
Published: January 24, 2019

REFERENCES

Bin, P., Huang, R., and Zhou, X. (2017). Oxidation resistance of the sulfur amino acids: methionine and cysteine. Biomed. Res. Int. *2017*, 9584932.

Bykov, V.J., Issaeva, N., Shilov, A., Hultcrantz, M., Pugacheva, E., Chumakov, P., Bergman, J., Wiman, K.G., and Selivanova, G. (2002). Restoration of the tumor suppressor function to mutant p53 by a low-molecular-weight compound. Nat. Med. *8*, 282–288.

Bykov, V.J., Zhang, Q., Zhang, M., Ceder, S., Abrahmsen, L., and Wiman, K.G. (2016). Targeting of mutant p53 and the cellular redox balance by APR-246 as a strategy for efficient cancer therapy. Front. Oncol. *6*, 21.

Caumanns, J.J., Wisman, G.B.A., Berns, K., van der Zee, A.G.J., and de Jong, S. (2018). ARID1A mutant ovarian clear cell carcinoma: a clear target for synthetic lethal strategies. Biochim. Biophys. Acta Rev. Cancer *1870*, 176–184.

Chipuk, J.E., Maurer, U., Green, D.R., and Schuler, M. (2003). Pharmacologic activation of p53 elicits Bax-dependent apoptosis in the absence of transcription. Cancer Cell *4*, 371–381.

Ding, L., Bailey, M.H., Porta-Pardo, E., Thorsson, V., Colaprico, A., Bertrand, D., Gibbs, D.L., Weerasinghe, A., Huang, K.L., Tokheim, C., et al. (2018). Perspective on oncogenic processes at the end of the beginning of cancer genomics. Cell *173*, 305–320.e10.

Gorrini, C., Harris, I.S., and Mak, T.W. (2013). Modulation of oxidative stress as an anticancer strategy. Nat. Rev. Drug Discov. *12*, 931–947.

Grellety, T., Laroche-Clary, A., Chaire, V., Lagarde, P., Chibon, F., Neuville, A., and Italiano, A. (2015). PRIMA-1(MET) induces death in soft-tissue sarcomas cell independent of p53. BMC Cancer *15*, 684.

Harris, I.S., Treloar, A.E., Inoue, S., Sasaki, M., Gorrini, C., Lee, K.C., Yung, K.Y., Brenner, D., Knobbe-Thomsen, C.B., Cox, M.A., et al. (2015). Glutathione and thioredoxin antioxidant pathways synergize to drive cancer initiation and progression. Cancer Cell *27*, 211–222.

Hirsch, F.R., Varella-Garcia, M., Bunn, P.A., Jr., Di Maria, M.V., Veve, R., Bremmes, R.M., Baron, A.E., Zeng, C., and Franklin, W.A. (2003). Epidermal growth factor receptor in non-small-cell lung carcinomas: correlation between gene copy number and protein expression and impact on prognosis. J. Clin. Oncol. *21*, 3798–3807.

Jones, S., Wang, T.L., Shih Ie, M., Mao, T.L., Nakayama, K., Roden, R., Glas, R., Slamon, D., Diaz, L.A., Jr., Vogelstein, B., et al. (2010). Frequent mutations of chromatin remodeling gene ARID1A in ovarian clear cell carcinoma. Science *330*, 228–231.

Kadoch, C., Hargreaves, D.C., Hodges, C., Elias, L., Ho, L., Ranish, J., and Crabtree, G.R. (2013). Proteomic and bioinformatic analysis of mammalian SWI/SNF complexes identifies extensive roles in human malignancy. Nat. Genet. *45*, 592–601.

Kanke, Y., Shimomura, A., Saito, M., Honda, T., Shiraishi, K., Shimada, Y., Watanabe, R., Yoshida, H., Yoshida, M., Shimizu, C., et al. (2018). Gene aberration profile of tumors of adolescent and young adult females. Oncotarget *9*, 6228–6237.

Lambert, J.M., Gorzov, P., Veprintsev, D.B., Soderqvist, M., Segerback, D., Bergman, J., Fersht, A.R., Hainaut, P., Wiman, K.G., and Bykov, V.J. (2009). PRIMA-1 reactivates mutant p53 by covalent binding to the core domain. Cancer Cell *15*, 376–388.

Lawrence, M.S., Stojanov, P., Mermel, C.H., Robinson, J.T., Garraway, L.A., Golub, T.R., Meyerson, M., Gabriel, S.B., Lander, E.S., and Getz, G. (2014). Discovery and saturation analysis of cancer genes across 21 tumour types. Nature *505*, 495–501.

Lehmann, S., Bykov, V.J., Ali, D., Andren, O., Cherif, H., Tidefelt, U., Uggla, B., Yachnin, J., Juliusson, G., Moshfegh, A., et al. (2012). Targeting p53 in vivo: a first-in-human study with p53-targeting compound APR-246 in refractory hematologic malignancies and prostate cancer. J. Clin. Oncol. *30*, 3633–3639.

Lord, C.J., and Ashworth, A. (2016). BRCAness revisited. Nat. Rev. Cancer *16*, 110–120.

Luchini, C., Veronese, N., Solmi, M., Cho, H., Kim, J.H., Chou, A., Gill, A.J., Faraj, S.F., Chaux, A., Netto, G.J., et al. (2015). Prognostic role and implications of mutation status of tumor suppressor gene ARID1A in cancer: a systematic review and meta-analysis. Oncotarget *6*, 39088–39097.

Matsuzawa, A., and Ichijo, H. (2008). Redox control of cell fate by MAP kinase: physiological roles of ASK1-MAP kinase pathway in stress signaling. Biochim. Biophys. Acta *1780*, 1325–1336.

Nishiumi, S., Kobayashi, T., Kawana, S., Unno, Y., Sakai, T., Okamoto, K., Yamada, Y., Sudo, K., Yamaji, T., Saito, Y., et al. (2017). Investigations in the possibility of early detection of colorectal cancer by gas chromatography/triple-quadrupole mass spectrometry. Oncotarget *8*, 17115–17126.

Ogiwara, H., Sasaki, M., Mitachi, T., Oike, T., Higuchi, S., Tominaga, Y., and Kohno, T. (2016). Targeting p300 addiction in CBP-deficient cancers causes synthetic lethality by apoptotic cell death due to abrogation of MYC expression. Cancer Discov. *6*, 430–445.

Oike, T., Ogiwara, H., Tominaga, Y., Ito, K., Ando, O., Tsuta, K., Mizukami, T., Shimada, Y., Isomura, H., Komachi, M., et al. (2013). A synthetic lethality-based strategy to treat cancers harboring a genetic deficiency in the chromatin remodeling factor BRG1. Cancer Res. *73*, 5508–5518.

Peng, X., Zhang, M.Q., Conserva, F., Hosny, G., Selivanova, G., Bykov, V.J., Arner, E.S., and Wiman, K.G. (2013). APR-246/PRIMA-1MET inhibits thioredoxin reductase 1 and converts the enzyme to a dedicated NADPH oxidase. Cell Death Dis. *4*, e881.

Sasaki, H., Sato, H., Kuriyama-Matsumura, K., Sato, K., Maebara, K., Wang, H., Tamba, M., Itoh, K., Yamamoto, M., and Bannai, S. (2002). Electrophile response element-mediated induction of the cystine/glutamate exchange transporter gene expression. J. Biol. Chem. *277*, 44765–44771.

Shen, J., Peng, Y., Wei, L., Zhang, W., Yang, L., Lan, L., Kapoor, P., Ju, Z., Mo, Q., Shih Ie, M., et al. (2015). ARID1A deficiency impairs the DNA damage checkpoint and sensitizes cells to PARP inhibitors. Cancer Discov. *5*, 752–767.

Steinherz, R., Tietze, F., Gahl, W.A., Triche, T.J., Chiang, H., Modesti, A., and Schulman, J.D. (1982). Cystine accumulation and clearance by normal and cystinotic leukocytes exposed to cystine dimethyl ester. Proc. Natl. Acad. Sci. U S A *79*, 4446–4450.

Tessoulin, B., Descamps, G., Moreau, P., Maiga, S., Lode, L., Godon, C., Marionneau-Lambot, S., Oullier, T., Le Gouill, S., Amiot, M., and Pellat-Deceunynck, C. (2014). PRIMA-1Met induces myeloma cell death independent of p53 by impairing the GSH/ROS balance. Blood *124*, 1626–1636.

Wang, P., Yu, W., Hu, Z., Jia, L., Iyer, V.R., Sanders, B.G., and Kline, K. (2008). Involvement of JNK/p73/NOXA in vitamin E analog-induced apoptosis of human breast cancer cells. Mol. Carcinog. *47*, 436–445.

Weng, M.S., Chang, J.H., Hung, W.Y., Yang, Y.C., and Chien, M.H. (2018). The interplay of reactive oxygen species and the epidermal growth factor receptor in tumor progression and drug resistance. J. Exp. Clin. Cancer Res. *37*, 61.

Wiegand, K.C., Shah, S.P., Al-Agha, O.M., Zhao, Y., Tse, K., Zeng, T., Senz, J., McConechy, M.K., Anglesio, M.S., Kalloger, S.E., et al. (2010). ARID1A mutations in endometriosis-associated ovarian carcinomas. N. Engl. J. Med. *363*, 1532–1543.

Wu, J.N., and Roberts, C.W. (2013). ARID1A mutations in cancer: another epigenetic tumor suppressor? Cancer Discov. *3*, 35–43.

Yoh, K., Seto, T., Satouchi, M., Nishio, M., Yamamoto, N., Murakami, H., Nogami, N., Matsumoto, S., Kohno, T., Tsuta, K., et al. (2016). Vandetanib in patients with previously treated RET-rearranged advanced non-small-cell lung cancer (LURET): an open-label, multicentre phase 2 trial. Lancet Respir. Med. *5*, 42–50.

Zeke, A., Misheva, M., Remenyi, A., and Bogoyevitch, M.A. (2016). JNK signaling: regulation and functions based on complex protein-protein partnerships. Microbiol. Mol. Biol. Rev. *80*, 793–835.

STAR★METHODS

KEY RESOURCES TABLE

REAGENT or RESOURCE	SOURCE	IDENTIFIER
Antibodies		
Rabbit Anti-beta-Actin Monoclonal Antibody, Unconjugated, Clone 13E5	Cell Signaling Technology	Cat# 4970; RRID: AB_2223172
beta-Actin (8H10D10) Mouse mAb antibody	Cell Signaling Technology	Cat# 3700; RRID: AB_2242334
p21 Waf1/Cip1 (12D1) Rabbit monoclonal antibody	Cell Signaling Technology	Cat# 2947; RRID: AB_823586
Mouse Anti-Human p53 (Pantropic) Monoclonal Antibody	Calbiochem	Cat# OP43-100UG; RRID: AB_213402
NFE2L2-human antibody	Abcam	Cat# ab62352; RRID: AB_944418
Noxa [114C307] antibody	GeneTex	Cat# GTX13654; RRID: AB_367453
xCT/SLC7A11 (D2M7A) Rabbit Antibody	Cell Signaling Technology	Cat# 12691; RRID: AB_2687474
JNK (D-2) antibody	Santa Cruz Biotechnology	Cat# sc-7345; RRID: AB_675864
p-JNK (G-7) antibody	Santa Cruz Biotechnology	Cat# sc-6254; RRID: AB_628232
ARID1A/BAF250A (D2A8U) Rabbit mAb	Cell Signaling Technology	Cat# 12354; RRID: AB_2637010
Brg1 (D1Q7F) antibody	Cell Signaling Technology	Cat# 49360; RRID: AB_2728743
Anti-NRF2 (D1Z9C) XP Rabbit monoclonal Antibody	Cell Signaling Technology	Cat# 12721; RRID: AB_2715528
RNA pol II antibody	Active Motif	Cat# 39097; RRID: AB_2732926
Anti-GCLC antibody [EP13475]	Abcam	Cat# ab190685
Monoclonal Mouse Anti-Human Ki-67 Antibody	Dako	Cat# GA626; RRID: AB_2687921
Cleaved Caspase-3 (Asp175) (5A1E) Rabbit mAb antibody	Cell Signaling Technology	Cat# 9664; RRID: AB_2070042
Cleaved PARP (Asp214) (D64E10) XP Rabbit mAb antibody	Cell Signaling Technology	Cat# 5625P; RRID: AB_10699460
Noxa antibody [114C307]	Abcam	Cat# ab13654; RRID: AB_300536
Mouse Anti-8-Hydroxy-2'-deoxyguanosine Monoclonal Antibody	Abcam	Cat# ab48508; RRID: AB_867461
Anti-ARID1A antibody produced in rabbit	Sigma-Aldrich	Cat# HPA005456; RRID: AB_1078205
anti-SLC7A11 (xCT) (EPR8290(2))	Abcam	Cat# ab175186; RRID: AB_2722749
Biological Samples		
Ovarian tumor samples	National Cancer Center Hospital or Kaname-cho Hospital	N/A
Ovarian cancer specimens	National Cancer Center Hospital and Jikei University Hospital	
Chemicals, Peptides, and Recombinant Proteins		
PRIMA-1	Sigma-Aldrich	Cat# P0069-5MG CAS: 5608-24-2
N-acetylcysteine (NAC)	Sigma-Aldrich	Cat# A7250-5G CAS: 616-91-1
L-Buthionine-sulfoximine (BSO)	Sigma-Aldrich	Cat# B2515-500MG CAS: 83730-53-4
glutathione monoethyl ester (GSH-MEE)	Sigma-Aldrich	Cat# G1404-25MG CAS: 92614-59-0
SP600125 (JNK inhibitor)	Sigma-Aldrich	Cat# S5567-10MG CAS: 129-56-6
L-Cystine dimethyl ester dihydrochloride (CC-DME)	Sigma-Aldrich	Cat# 857327-5G CAS: 32854-09-4
APR-246 (PRIMA-1MET)	Cayman	Cat# 9000487 CAS: 5291-32-7
sulfasalazine	Cayman	Cat# 15025 CAS: 599-79-1
compound 968	Cayman	Cat# 17199 CAS: 311795-38-7
6-amiononicotinamide	Sigma-Aldrich	Cat# A68203-1G CAS: 329-89-5
DMEM/F-12	Wako	Cat# 048-29785
fetal bovine serum	GIBCO	Cat# 10270106
Penicillin-Streptomycin	Wako	Cat# 16823191
Trypsin-EDTA (0.25%), phenol red	Wako	Cat# 201-16945
Polybrene	Santa Cruz Biotechnology	Cat# sc-134220
Blasticidin S Hydrochloride	Wako	Cat# 029-18701

(*Continued on next page*)

Continued

REAGENT or RESOURCE	SOURCE	IDENTIFIER
Puromycin	Sigma-Aldrich	Cat# P7255-25MG
Dimethyl sulfoxide	Wako	Cat# 049-07213
Formaldehyde	Wako	Cat# 061-00416
Lipofectamine 3000 Transfection Reagent	Thermo Fisher Scientific	Cat# L3000015
Lipofectamine RNAiMAX Transfection Reagent	Thermo Fisher Scientific	Cat# 13778150
Doxycycline	Sigma-Aldrich	Cat# D9891-25G
Ficoll-Paque PLUS	GE Healthcare	Cat# 17144003
Matrigel	BD Biosciences	Cat# BD 354234
proteinase inhibitor cocktail	Active Motif	Cat# 37491
phosphatase inhibitor cocktail	Active Motif	Cat# 37493
M-PER Mammalian Protein Extraction Regent Buffer	Thermo Scientific	Cat# 78505
OCT compound	Tissue Tek	Cat# 25608-930
Critical Commercial Assays		
RNeasy Mini Kit (RNA extraction)	Qiagen	Cat# 74106
MycoAlert	Lonza	Cat# LT07-318
EasySep Human EpCAM Positive Selection Kit	STEMCELL	Cat# 18356
Annexin V–FITC/PI Apoptosis Detection Kit	Sigma-Aldrich	Cat# 11858777001
CellTiter-Glo Luminescent Cell Viability	Promega	Cat# G7571
GSH/GSSG-Glo™ Assay	Promega	Cat# V6611
GSH-Glo™ Assay	Promega	Cat# V6911
ROS-Glo™ H2O2 Assay	Promega	Cat# G8820
Caspase-Glo® 3/7 Assay	Promega	Cat# G8091
Thioredoxin (TrxR) Reductase Assay Kit	Abcam	Cat# ab83463
Human Cell Stress Array	R&D Systems	Cat# ARY018
SuperPrep® Cell Lysis & RT Kit for qPCR	TOYOBO	Cat# SCQ-101
SuperPrep®/THUNDERBIRD® Probe qPCR Set	TOYOBO	Cat# QPS-101
SuperPrep®/THUNDERBIRD® SYBR qPCR Set	TOYOBO	Cat# QPS-201
PVDF Blocking Reagent for Can Get Signal	TOYOBO	Cat# NYPBR01
Can Get Signal Solution 1	TOYOBO	Cat# NKB-201
Western Lightning ECL Pro	Perkin Elmer	Cat# NEL120001EA
ChIP-IT Express Enzymatic kit	Active Motif	Cat# 53009
Low Input Quick Amp Labeling Kit, one-color	Agilent Technologies	Cat# 5190-2306
Gene Expression Hybridization Kit	Agilent Technologies	Cat# 5188-5242
Agilent SureSelect kit NCC Oncopanel	Agilent Technologies	Cat# 931196
Deposited Data		
Whole gene expression assay	This study	GEO: GSE122925 and , GSE122926
Experimental Models: Cell Lines		
TOV21G	ATCC	CRL-11730
RMG-I	JCRB	JCRB0172
OVISE	JCRB	JCRB1043
HEC-265	JCRB	JCRB1142
HEC-151	JCRB	JCRB1122
KKU-100	JCRB	JCRB1568
KKU-055	JCRB	JCRB1551
JHUEM-2	RCB	RCB1551
2008	Drs. S.B. Howell and E. Reed	N/A
A2780	Drs. S.B. Howell and E. Reed	N/A
HCT116	Horizon Discovery	N/A
HCT116 ARID1A-KO (Q456X/Q456X)	Horizon Discovery	HD 104-049

(*Continued on next page*)

Continued

REAGENT or RESOURCE	SOURCE	IDENTIFIER
Oligonucleotides		
SMARTpool: ON-TARGETplus NOXA (PMAIP1) siRNA	Dharmacon	Gat# L-005275-00
SMARTpool: ON-TARGETplus GSR siRNA	Dharmacon	Gat# L-009647-00
SMARTpool: ON-TARGETplus GSS siRNA	Dharmacon	Gat# L-009586-00
SMARTpool: ON-TARGETplus GCLC siRNA	Dharmacon	Gat# L-009212-00
SMARTpool: ON-TARGETplus GLS siRNA	Dharmacon	Gat# L-004548-01
SMARTpool: ON-TARGETplus GLS2 siRNA	Dharmacon	Gat# L-012500-01
SMARTpool: ON-TARGETplus SLC7A11 siRNA	Dharmacon	Gat# L-007612-01
SMARTpool: ON-TARGETplus SLC1A4 siRNA	Dharmacon	Gat# L-007428-01
SMARTpool: ON-TARGETplus SLC1A5 siRNA	Dharmacon	Gat# L-007429-00
SMARTpool: ON-TARGETplus PKM siRNA	Dharmacon	Gat# L-006781-00
SMARTpool: ON-TARGETplus PHGDH siRNA	Dharmacon	Gat# L-009518-00
SMARTpool: ON-TARGETplus TXNRD1 siRNA	Dharmacon	Gat# L-008236-00
SMARTpool: ON-TARGETplus TXNRD2 siRNA	Dharmacon	Gat# L-009089-00
SMARTpool: ON-TARGETplus TXNRD3 siRNA	Dharmacon	Gat# L-023590-00
SMARTpool: ON-TARGETplus G6PD siRNA	Dharmacon	Gat# L-008181-02
SMARTpool: ON-TARGETplus ME1 siRNA	Dharmacon	Gat# L-009348-00
SMARTpool: ON-TARGETplus SOD1 siRNA	Dharmacon	Gat# L-008364-00
SMARTpool: ON-TARGETplus SOD2 siRNA	Dharmacon	Gat# L-009784-00
SMARTpool: ON-TARGETplus SOD3 siRNA	Dharmacon	Gat# L-009741-00
SMARTpool: ON-TARGETplus IDH1 siRNA	Dharmacon	Gat# L-008294-01
SMARTpool: ON-TARGETplus IDH2 siRNA	Dharmacon	Gat# L-004013-01
TaqMan® Gene Expression Assays GCLC	Applied biosystems	Gat# Hs00155249_m1
TaqMan® Gene Expression Assays GSS	Applied biosystems	Gat# Hs00609286_m1
TaqMan® Gene Expression Assays NOXA (PMAIP1)	Applied biosystems	Gat# Hs00921938_m1
TaqMan® Gene Expression Assays NRF2 (NFE2L2)	Applied biosystems	Gat# Hs00975961_g1
Primer for ChIP Forward: SLC7A11-1182-1099-F (5'-TCAGAAGCTTATTTAATGGTGCG-3')	This study	N/A
Primer for ChIP Reverse: SLC7A11-1182-1099-R (5'-GTGGTTTTGGATTCAGTGAGAAG-3')	This study	N/A
Primer for ChIP Forward: SLC7A11-297-241-F (5'-CAGCTTTTGTTGCTCACTACG-3')	This study	N/A
Primer for ChIP Reverse: SLC7A11-297-241-R (5'-TCGGAACAGACCTTCCCAG-3')	This study	N/A
Primer for ChIP Forward: SLC7A11-14_79-F (5'-GAGGAAGCTGAGCTGGTTTG-3')	This study	N/A
Primer for ChIP Reverse: SLC7A11-14_79-R (5'-GCATCGTGCTCTCAATTCTC-3')	This study	N/A
Primer for ChIP Forward: SLC7A11_71_190-F (5'-GCACGATGCATACACAGGTG-3')	This study	N/A
Primer for ChIP Reverse: SLC7A11_71_190-R (5'-CCTCTGCTTTCAGACTGTCT-3')	This study	N/A
Primer for ChIP Forward: SLC7A11_972_1070-F (5'- CGGAGTGTTCAGCAGAAGTC-3')	This study	N/A
Primer for ChIP Reverse: SLC7A11_972_1070-R (5'- GAGGTGACAAGCACATGAAC-3')	This study	N/A
Recombinant DNA		
pLOC-GCLC	Thermo Scientific	OHS5897_202616616
pLOC-SLC7A11	Thermo Scientific	OHS5898_219582558
pLOC-NRF2	Thermo Scientific	OHS5900-202624558
pLenti-puro-ARID1A	Addgene	#39478

(*Continued on next page*)

Continued

REAGENT or RESOURCE	SOURCE	IDENTIFIER
Software and Algorithms		
Multi Gauge software	Fujifilm	N/A
GuavaSoft software (v. 2.7)	Millipore	http://www.merckmillipore.com
Feature Extraction software	Agilent Technologies	https://www.agilent.com
GeneSpring GX12.6	Agilent Technologies	https://www.agilent.com
Burrows-Wheeler Aligner Multi-Vision software package	Bio-BWA	http://bio-bwa.sourceforge.net/
GCMS solution software	Shimadzu	https://www.ssi.shimadzu.com
GATK Somatic IndelDetector	Broad institute	http://archive.broadinstitute.org/cancer/cga/indelocator
Microsoft Excel	Microsoft	https://products.office.com/en/excel

CONTACTS FOR REAGENT AND RESOURCE SHARING

Further information and requests for resources and reagents should be directed to and will be fulfilled by the Lead Contact, Takashi Kohno (tkkohno@ncc.go.jp).

EXPERIMENTAL MODEL AND SUBJECT DETAILS

Establishment of Ovarian Cancer PDCs

Tumor samples and ascites were obtained from four ovarian cancer patients who underwent surgery or cell-free and concentrated ascites reinfusion therapy at the National Cancer Center Hospital or Kaname-cho Hospital (Tokyo, Japan) and were cultured *in vitro*. This protocol was approved by the Institutional Review Board of the National Cancer Center (Tokyo, Japan), and informed consent was obtained from the patients. To establish CCC0219 and CCC1216 PDCs, patient ascites (24 ml) were diluted in two volumes of PBS containing 2 mM EDTA, layered over 15 ml Ficoll-Paque PLUS (GE Healthcare), and centrifuged at 2200 rpm for 30 min. The interphase mononuclear layer was transferred to a fresh conical tube and washed twice with PBS containing 2 mM EDTA. Epithelial cells were labeled magnetically with microbeads conjugated to a monoclonal human epithelial antigen-125 antibody (EasySep Human EpCAM Positive Selection Kit, STEMCELL Technologies). Epithelial antigen-125–positive cells were collected by magnetic selection and cultured in DMEM/F-12 supplemented with 10% FBS. To establish NOVC-1C and NOVC-4C PDCs, whole ascetic cells were pelleted by centrifugation at 1500 rpm for 5 min at room temperature and then incubated in hemolysis buffer (0.75% NH_4Cl and 17 mM Tris-HCl, pH 7.65) for 10 min. After centrifugation, pellets were washed with PBS and cultured in RPMI 1640 containing 10% FBS for 1 week. Thereafter, the culture medium was replaced with DMEM containing 10% FBS to remove lymphocytes, and cells were cultured for another week. Adherent cells were cultured in RPMI 1640 containing 10% FBS for several weeks, exchanging the medium once per week, until multiple colonies appeared. If needed, cultured cells were treated repeatedly with 0.05% trypsin-EDTA for a short duration to remove fibroblasts or other cell types such as mesothelial cells. The culture was passaged when colonies became dense. The ARID1A expression status was confirmed by immunoblot analysis.

Mouse Xenograft Model

All mouse experiments were approved by the National Cancer Center (NCC) animal Ethical Committee. Cells were counted and re-suspended in a 1:1 mixture of 100 μl culture medium and 100 μl Matrigel (BD Biosciences) on ice. Thereafter, cells (RMG-I: 2×10^6 cells/mouse; TOV21G: 2×10^5 cells/mouse for ARP-246 treatment and 1×10^6 cells/mouse for BSO treatment; OVISE: 2×10^6 cells/mouse; TOV21G-shNT: 2×10^5 cells/mouse; and TOV21G-shGCLC: 2×10^5 cells/mouse) were injected subcutaneously into the flank of 6-week-old female BALB/c-nu/nu mice (CLEA and Charles River). In the subcutaneous model, once the tumors were palpable (about 3–14 days after implantation), mice were randomly divided into two groups. In the drug treatment group, mice were injected intraperitoneally with either PBS or compounds [APR-246 (50 mg/kg), PRIMA-1 (25 mg/kg), or BSO (750 mg/kg)] once daily for 12–14 days. In the doxycycline (Dox) treatment study, TOV21G-shNT cells and TOV21G-shGCLC cells were injected into the flanks of 6-week-old female BALB/c-nu/nu mice. Once the tumors were palpable (13 days after implantation), mice were randomly divided into two groups and fed a diet containing Dox (625 ppm) or a control diet. In other experiments, TOV21G-shNT cells and TOV21G-shGCLC cells were treated with Dox (0.5 μg/ml) for 4 days and then injected into the flank of 6-week-old female BALB/c-nu/nu mice. The mice were then fed a diet containing Dox (625 ppm) or a control diet. Tumor growth was measured every several days using calipers. The volume of implanted tumors was calculated using the formula $V = L \times W^2/2$, where V is volume (mm^3), L is the largest diameter (mm), and W is the smallest diameter (mm). At the end of the experiment, mice were sacrificed in accordance with standard protocols.

Cell Lines

Cells were maintained in a humidified incubator containing 5% CO_2 at 37°C in DMEM/F-12 (Wako) supplemented with 10% fetal bovine serum (FBS; Gibco/Life Technologies), 2 μmol/l glutamine, 100 U/ml penicillin, and 100 μg/mL streptomycin (Wako). TOV21G cells were obtained from the American Type Culture Collection (ATCC). RMG-I, OVISE, HEC-265, HEC-151, KKU-100, and KKU-055 cells were obtained from the Japanese Collection of Research Bioresources (JCRB) Cell Bank. JHUEM-2 cells were obtained from the Riken Cell Bank (RCB). 2008 and A2780 cells were provided by Drs. S.B. Howell and E. Reed. *ARID1A*-KO (Q456X/Q456X) and parental HCT116 cells were purchased from Horizon Discovery. The cell lines were authenticated by verifying alterations of multiple cancer-related genes via sequencing. Cells were used for functional experiments after less than 3 months of passaging post-receipt. All cell lines tested negative for mycoplasma by MycoAlert (Lonza).

Generation of shRNA- and cDNA-Expressing Lentiviruses and Virus-Infected Cells

The shRNA-expressing lentiviral vectors pGIPZ (shNT, OHS4346; shp53, RHS4430-200289946) (Open Biosystems) and pTRIPZ (shNT, OHS5832; shGCLC #3, RHS4946_200777182), the cDNA-expressing lentiviral vectors (pLOC-GCLC, OHS5897_202616616; pLOC-SLC7A11, OHS5898_219582558; pLOC-NRF2, OHS5900-202624558) (all from ThermoFisher Scientific), (pLenti-puro-ARID1A, #39478) (Addgene), and packaging plasmids (psPAX2: #12260 and pMD2.G: #12259) (Addgene) were used for constitutive expression of shRNA or cDNAs. To generate virus, 293LTV cells were transfected with lentiviral plasmids and packaging plasmids using Lipofectamine 3000 (Invitrogen/ThermoFisher Scientific). On the following day, the medium was replaced with fresh growth medium and lentivirus-containing supernatants were harvested and concentrated by centrifugation. To establish cells infected with viral constructs, cells were transduced with lentiviral vectors and then incubated for 7–14 days in growth medium containing 2 μg/ml puromycin (Sigma-Aldrich) or 20 μg/ml blasticidin (Wako).

METHOD DETAILS

Drug Library Screen

ARID1A-WT and *ARID1A*-KO HCT116 cancer cells were used for screening assays. Cells were seeded in 96-well plates, incubated for 24 hr, and then treated with the drug at a concentration of 0.01, 0.1, 1, or 10 μM [SCADS Inhibitor Kit, including 334 compounds (Table S1)]. Cell viability was assessed after 5 days using the CellTiter-Glo Luminescent Cell Viability Assay (Promega). Luminescence was measured using an Envision Multi-label plate reader (PerkinElmer). The luminescence reading was used to determine the cell viability relative to that of cells treated with solvent (DMSO). Candidate compounds were considered if viability of *ARID1A*-KO cells was less than 40% that of *ARID1A*-WT cells was more than 80%.

Cell Viability Assay

Cell viability was examined by measuring the cellular ATP level using the CellTiter-Glo Luminescent Cell Viability Assay (Promega). To measure cell viability after siRNA-mediated knockdown, cell lines were transfected with siRNAs (25 nM) using Lipofectamine RNAiMAX. After 48 hr, cells were trypsinized and repeatedly transfected with siRNAs (25 nM) using Lipofectamine RNAiMAX. Cells were trypsinized after a further 48 hr, counted, and reseeded at the specified density in 96-well plates. To measure cell viability after drug treatment, cells were trypsinized, counted, reseeded at the specified density in 96-well plates, and exposed to the indicated concentrations of drugs. Cell viability was measured using the CellTiter-Glo Luminescent Cell Viability Assay. Luminescence was measured using an Envision Multi-label plate reader (PerkinElmer).

Colony Formation Assay

The effect of drug treatment on cancer cell survival was evaluated in a colony formation assay. Cells were trypsinized, counted, reseeded at the specified density in 12-well plates, exposed to the indicated concentrations of drugs for 10–14 days, and fixed for 10 min in 50% (v/v) methanol containing 0.01% (w/v) crystal violet. Images were taken on LAS-3000 Imaging System (Fujifilm) and colonies were counted using Multi Gauge software.

Annexin V/Propidium Iodide (PI) Staining Assay

The Annexin V–FITC/PI Apoptosis Detection Kit (Sigma-Aldrich) was used to detect apoptotic cells. Briefly, the cell pellet was suspended in 1× binding buffer and then incubated with Annexin V–FITC and PI in the dark for 10 min. Fluorescence was analyzed on a Guava flow cytometer (Millipore). Data were analyzed using GuavaSoft software (v. 2.7). Relative ratios of the Annexin V-positive fraction in treated samples were normalized against untreated samples.

Detection of, GSH, ROS and Cleaved Caspase-3/7 in Cell Lines

GSH, ROS and apoptosis were detected using the GSH/GSSG-Glo Assay (Promega) and/or the GSH-Glo Assay (Promega), the ROS-Glo Assay (Promega), and the Caspase-Glo 3/7 Assay, respectively. To measure levels of GSH, ROS and apoptosis after drug treatment, cells were trypsinized, counted, reseeded at the specified density in 96-well plates and exposed to the indicated concentrations of drugs. After 16–48 hr, luminescence was measured using an Envision Multi-label plate reader (PerkinElmer). To measure levels of GSH and ROS after siRNA-mediated knockdown, cell lines were transfected with siRNAs (25 nM) using Lipofectamine RNAiMAX. After 48 hr, cells were trypsinized and transfected repeatedly with siRNAs (25 nM) using Lipofectamine RNAiMAX. Cells

were trypsinized after a further 48 hr, counted, and reseeded at the specified density in 96-well plates. After 72–120 hr, luminescence was measured using an Envision Multi-label plate reader (PerkinElmer). Cell viability was also measured using the CellTiter-Glo Luminescent Cell Viability Assay (Promega). Caspase-3/7, GSH, and ROS levels were normalized against cell viability. The GSH/GSSG ratio was calculated as the GSH-GSSG signal divided by the GSSG/2 signal. Relative signal ratios in treated samples were normalized against untreated samples.

Detection of GSH in Tumor Samples

GSH was detected using the GSH-Glo Assay (Promega). Tumor samples derived from xenografts were weighed and washed with PBS. The tumor samples were mixed with 50 μl of PBS and homogenized using a Mini Cordless Grinder (Funakoshi). PBS (950 μl) was added to homogenized tumor samples and centrifuged at 4°C for 10 min at 15,000 rpm. Tumor extract and 2X GSH-Glo Reagent (25 μl of each) were mixed in white 96-well plates (Greiner) and incubated for 30 min at room temperature. Luciferin Detection Reagent (50 μl) was added and the samples were incubated for 15 min at room temperature. Luminescence was measured using an Envision Multi-label plate reader (PerkinElmer). GSH signal intensities per 1 mg of tumor sample were calculated. Relative GSH ratios were normalized against untreated samples (without APR-246 or Dox).

Detection of TrxR Activity

TrxR activity including TrxR1, TrxR2 and TrxR3 was measured using the Thioredoxin Reductase Assay Kit (Abcam). Cells were trypsinized, counted, reseeded at the specified density in 10 cm dishes and exposed to the indicated concentrations of APR-246. After 24 hr, cells were washed with cold PBS and lysed with buffer containing a proteinase inhibitor. After centrifugation, the supernatant was supplemented with a TrxR inhibitor and incubated for 20 min at 25°C. Absorbance was measured using an Envision Multi-label plate reader (PerkinElmer). Relative TrxR ratios were normalized against untreated samples.

Cell Stress Profiling by Antibody Array

Antibody array analysis was conducted using the Human Cell Stress Array (R&D Systems). For whole-cell extraction, 1 x 10^7 cells were harvested, washed with PBS, lysed in Lysis Buffer 6 supplemented with a proteinase inhibitor cocktail and a phosphatase inhibitor cocktail (Active Motif), incubated for 30 min on ice, and centrifuged at 4°C for 10 min at 15,000 rpm. Whole-cell lysates (1 ml) were mixed with 0.5 ml of Array Buffer 4 and 20 μl of reconstituted Detection Antibody Cocktail for 1 hr at room temperature. These samples were added to membranes blocked with Array Buffer 4. After incubation overnight at 4°C, the membranes were washed twice with 1× Wash Buffer and rinsed with distilled water and then dried. Diluted streptavidin-HRP (2 ml) was added and the membrane was incubated for 30 min at room temperature and then was washed with 1× Wash Buffer. Chemi Reagent Mix was applied evenly to the membrane and incubated for 1 min. Chemiluminescence signals were measured using LAS-3000 Imaging System (Fujifilm). Signal intensities were measured using Multi Gauge software. The ratios of signal intensities in cells treated with 40 μM APR-246 for 24 hr were calculated relative to the corresponding intensities in untreated cells.

Transcriptomic Profiling by Microarray

Total RNA was extracted using the Qiagen RNeasy kit. The integrity of extracted RNA was confirmed by NanoDrop spectrophotometry (NanoDrop Technologies). Total RNA was reverse-transcribed using the Agilent Low Input Quick Amp Labeling Kit (Agilent Technologies). cDNA was hybridized for 16 hr at 65°C on duplicate Agilent microarrays (SurePrint G3 Human Gene Expression 8 × 60K Ver.1.0, G4851: 42405 probes) using the Gene Expression Hybridization Kit (Agilent Technologies). After the arrays were washed using the Gene Expression Wash Pack (Agilent Technologies), data were extracted using an Agilent scanner. The arrays were analyzed initially using Feature Extraction software (Agilent Technologies). A quantitative signal and qualitative detection call were generated for each sample and transcript.

Data files were subsequently analyzed, normalized, and compared using GeneSpring GX12.6 (Agilent Technologies). Raw expression data of 42,545 probe sets on SurePrint G3 Human Gene Expression arrays were processed and $\log_2$-transformed. Expression data for each sample were normalized against median expression levels in the control condition. Genes were grouped according to fold changes. All raw microarray data files have been deposited in the Gene Expression Omnibus (GEO: GSE122925 and GSE122926).

Quantitation of mRNA

mRNA was extracted and cDNA was synthesized using the SuperPrep®Cell Lysis & RT Kit for qPCR (TOYOBO). Aliquots of cDNA were subjected to quantitative PCR using the SuperPrep/THUNDERBIRD Probe qPCR Set (TOYOBO) and TaqMan Gene Expression Assays (Life Technologies). The following gene-specific primer/probe sets were used: NOXA (PMAIP1) (Hs00560402_m1), NRF2 (NFE2L2) (Hs00975961_g1), GCLC (Hs00155249_m1), GSS (Hs00609286_m1), and SLC7A11 (Hs00921938_m1). PCR was performed in an ABI StepOnePlus Real-Time PCR System (Life Technologies) under the following conditions: denaturation at 95°C for 15 s, followed by annealing and extension at 60°C for 30 s (40 cycles). For each sample, the mRNA levels of target genes were normalized against levels of GAPDH mRNA. The target/GAPDH ratios were then normalized against those in control samples using the $2^{-\Delta\Delta Ct}$ method.

Immunoblot Analysis

For whole-cell extraction, 5×10^5 cells were harvested, washed with PBS, lysed in NETN420 buffer [20 mM Tris-HCl (pH 7.5), 420 mM NaCl, 0.5% NP-40, and 1 mM EDTA] supplemented with a proteinase inhibitor cocktail and a phosphatase inhibitor cocktail (Active Motif), incubated for 30 min on ice, and centrifuged at 4°C for 10 min at 15,000 rpm. The soluble fractions of whole-cell lysates were mixed with SDS sample buffer. For cell extraction including the membrane fraction to detect SLC7A11, cells were harvested, washed with PBS, lysed in M-PER Mammalian Protein Extraction Regent Buffer (ThermoFisher Scientific) supplemented with a proteinase inhibitor cocktail and a phosphatase inhibitor cocktail (Active Motif), incubated for 10 min on ice, and centrifuged at 4°C for 10 min at 15,000 rpm. The soluble fractions were mixed with SDS sample buffer. Tumor samples derived from xenografts were weighed and washed with PBS. The tumor samples (10 mg) were mixed with 50 μl of NETN420 buffer supplemented with a proteinase inhibitor cocktail and a phosphatase inhibitor cocktail (Active Motif) and homogenized using a Mini Cordless Grinder (Funakoshi). The homogenized tumor samples were diluted in an additional 450 μl of NETN420 buffer, incubated for 30 min on ice, and centrifuged at 4°C for 10 min at 15,000 rpm. The soluble fractions of whole-cell lysates were mixed with SDS sample buffer. Proteins were separated by SDS-PAGE, transferred to PVDF membranes, and immunoblotted with the indicated antibodies. β-actin was used as a loading control. Membranes were blocked overnight at 4°C or for 1 hr at 25°C with PVDF Blocking Reagent for Can Get Signal (TOYOBO) and then probed with Can Get Signal Solution 1 (TOYOBO) containing primary antibodies. After washing with TBS containing 0.1% Tween 20, the membranes were incubated with TBS containing 0.1% Tween 20, 1% BSA, and horseradish peroxidase-conjugated anti-mouse or anti-rabbit secondary antibodies, and visualized using Western Lightning ECL Pro (Perkin Elmer). Chemiluminescence signals were measured using LAS-3000 Imaging System (Fujifilm). Signal intensities were measured using Multi Gauge software. The protein levels of GCLC were normalized against the levels of β-actin. The GCLC/β-actin ratios were then normalized against those in control samples without Dox treatment. Data are expressed as the mean ± SEM (n = 6). The following antibodies were used for immunoblotting: GCLC (Abcam, ab190685), NRF2 (Abcam, ab62352), p53 (Calbiochem, OP43), β-actin (CST, 4790), ARID1A (CST, 12354), BRG1 (CST, 49360), SLC7A11 (CST, 12691), NOXA (CST, 14766), p21 (CST, 2947), JNK (Santa Cruz Biotechnology, sc-7345), and phospho-JNK (Santa Cruz Biotechnology, sc-6254).

ChIP Assay

1×10^6 cells were harvested 24 hr after seeding and treated with 1% formaldehyde for 10 min at room temperature to crosslink proteins to DNA. Glycine (0.125 M) was added to stop the crosslinking process. ChIP assays were performed using the ChIP-IT Express Enzymatic kit (Active Motif) and antibodies against ARID1A (CST, 12354), BRG1 (CST, 49360), NRF2 (CST, 12721) or RNAPII (Active Motif, 39097). Purified DNA was subjected to quantitative PCR using the SuperPrep/THUNDERBIRD SYBR qPCR Set (TOYOBO) and the following primer pairs: SLC7A11-1182-1099-F (5'-TCAGAAGCTTATTTAATGGTGCG-3') and SLC7A11-1182-1099-R (5'-GTGGTTTTGGATTCAGTGAGAAG-3'); SLC7A11-297-241-F (5'-CAGCTTTTGTTGCTCACTACG-3') and SLC7A11-297-241-R (5'-TCGGAACAGACCTTCCCAG-3'); SLC7A11-14_79-F (5'-GAGGAAGCTGAGCTGGTTTG-3') and SLC7A11-14_79-R (5'-GCATCGTGCTCTCAATTCTC-3'); SLC7A11_71_190-F (5'-GCACGATGCATACACAGGTG-3') and SLC7A11_71_190-R (5'-CCTCTGCTTTCAGACTGTCT-3'); and SLC7A11_972_1070-F (5'- CGGAGTGTTCAGCAGAAGTC-3') and SLC7A11_972_1070-R (5'- GAGGTGACAAGCACATGAAC-3'). The PCR conditions were as follows: denaturation at 95°C for 15 s, followed by annealing and extension at 60°C for 60 s (45 cycles). PCR was performed on an ABI StepOnePlus Real-Time PCR System (Life Technologies). Protein enrichment was expressed as a percentage of input.

Metabolome Analysis

Metabolites were extracted from 2×10^6 cells. Culture medium was removed, and cells were washed twice with 5% mannitol solution (8 ml and then 4 ml) and then treated with 800 μl methanol and 150 μl Milli-Q water containing 5 μg 2-isopropylmalic acid as an internal control. The metabolite extract was transferred to a microfuge tube and dried using a Spin Dryer (TAITEC). Derivatization in the solid phase was conducted as described below. The solid phase cartridge Presh-SPE AOS was supplied by AiSTI SCIENCE (Wakayama). Cell extract was mixed with 200 μl Milli-Q water and 800 μl acetonitrile and incubated at 37°C for 30 min. After centrifugation at 14,000 rpm for 5 min at 4°C the supernatant was transferred to a new tube. The derivatization conditions were 3 min of methoximation with 5 μl of >5% methoxyamine solution and 10 min of trimethylsilylation with 25 μl N-methyl-N-trimethylsilyl-trifluoroacetamide. Derivatized analytes were effectively eluted with 100 μl n-hexane, and 1.0 μl of the derivatized solution was injected into the gas chromatograph/mass spectrometer GCMS-TQ8050 (Shimadzu).

Metabolome analysis was performed on a GCMS-TQ8050 equipped with a BPX-5 capillary column (internal diameter: 30 m × 0.25 mm; film thickness: 0.25 μm; SEG, Victoria). Parameter setting was described previously (Nishiumi et al., 2017). During GCMS-TQ8050 analysis, the inlet temperature was kept at 250°C and helium was used as a carrier gas at a constant flow rate of 39.0 cm per sec. The injector split ratio was set to 1:10. The GC column temperature was programmed to remain at 60°C for 2 min and then to rise from 60°C to 330°C at a rate of 15°C per min, before being kept at 330°C for 3 min. The total GC run time was 23 min. The transfer-line and ion-source temperatures were 280°C and 200°C, respectively. The ionization voltage was 70 eV. Argon gas was used as a collision-induced dissociation gas. Metabolites were detected using the Smart Metabolites Database (Shimadzu), which contains the relevant MRM method file and data regarding the GC analytical conditions, MRM parameters, and retention index employed for metabolite measurements. The Automatic Adjustment of Retention Time (AART) function of GCMS solution software (Shimadzu) and a standard alkane series mixture (C7 to C33) were used to correct the retention time. Peaks

were identified automatically and confirmed manually based on the specific precursor and product ions and the retention time. Relative cysteine ratios were normalized against ARID1A-proficient cells.

Targeted and Whole-Exome Sequencing

Targeted sequencing was conducted using 1.0 μg DNA extracted from cultured cancer cells. Targeted genome capture was performed using the Agilent SureSelect kit NCC Oncopanel (931196). Sequencing was performed on the Illumina NextSeq platform using 150 bp paired-end reads (Illumina). Basic alignment and sequence quality control were conducted using the Picard and Firehose pipelines. Reads were aligned against the reference human genome from the UCSC human genome 19 (hg19) using the Burrows-Wheeler Aligner Multi-Vision software package. Duplicate reads were generated during PCR; therefore, paired-end reads that aligned to the same genomic positions were removed using SAMtools. Somatic single-nucleotide variants were called by the MuTect program, which applies a Bayesian classifier to allow detection of somatic mutations with low allele frequencies. Somatic insertion/deletion mutations (indels) were called using the GATK Somatic IndelDetector (http://archive.broadinstitute.org/cancer/cga/indelocator).

Immunohistochemistry

Eleven patients were diagnosed with ovarian cancer and underwent surgery at the National Cancer Center Hospital (NCCH), Tokyo, Japan, or at the Jikei University Hospital (JUH), Tokyo, Japan. None of the 11 patients had received any pre-surgical treatment. This study was approved by the Institutional Review Board of the National Cancer Center (Tokyo, Japan) and Jikei University, and informed consent was obtained from the patients. Ovarian tumors were diagnosed in accordance with the International Federation of Gynecology and Obstetrics (FIGO) guidelines and classified according to the World Health Organization (WHO) classification system. *ARID1A* mutations were determined by target and whole-exome sequencing, as described previously (Kanke et al., 2018).

Formalin-fixed, paraffin-embedded ovarian cancer clinical specimens and TOV21G xenografts were deparaffinized and representative whole 4-μm-thick sections were analyzed by IHC. TOV21G-shGCLC xenografts were embedded in OTC compound (25608-930; Tissue-Tek) and stored at -80°C. The samples were removed from the freezer and equilibrated at -20°C for approximately 15 minutes before sectioning. Tissue sections (6 μm thick) were placed on positively charged slides, dried, and fixed for 15 minutes at room temperature in 3% formaldehyde, followed by 5 minutes in methanol at −20°C. After fixation, representative sections were analyzed by IHC. Tissue sections were stained using antibodies against Ki-67 (MIB-1) (GA62661-2, 1:100 dilution; Dako), cleaved caspase-3 (5A1E) (9664, 1:200 dilution; CST), cleaved PARP (D64E10) (5625, 1:100 dilution; CST), NOXA (114C307) (ab13654, 1:2000 dilution; Abcam), 8-hydroxy-2'-deoxyguanosine (N45.1) (ab48508, 1:500 dilution; Abcam), ARID1A (HPA005456, 1:2000 dilution; Sigma-Aldrich), and anti-SLC7A11 (xCT) (ab175186, 1:400 dilution; Abcam). All IHC staining was performed using a Dako autostainer Link48 (Dako).

Immunohistochemical staining for 8-OHdG was further evaluated by a semiquantitative approach used to assign a histological score (H-score) to tumor samples (Hirsch et al., 2003). First, membrane staining intensity (0, 1+, 2+, or 3+) was determined for each cell in a fixed field. The H-score was assigned using the following formula: [1 × (% cells 1+) + 2 × (% cells 2+) + 3 × (% cells 3+)]. The final score, ranging from 0 to 300, gives more relative weight to higher-intensity membrane staining in a given tumor sample. The percentage of NOXA-, cleaved caspase-3-, cleaved PARP- and Ki67-positive cells (of the total number of cells) in each slide were counted.

QUANTIFICATION AND STATISTICAL ANALYSIS

Statistical Analysis

Statistical analyses were performed using Microsoft Excel. Data are expressed as the mean ± SD or mean ± SEM, as indicated in the figure legends. The sample size (n) is indicated in the figure legends and represents biological replicates. Statistical significance was evaluated using the two-tailed Student's *t*-test. Statistically significant differences are indicated by asterisks as follows: *$p < 0.05$, **$p < 0.01$, and ***$p < 0.001$.

DATA AND SOFTWARE AVAILABILITY

All raw microarray data files have been deposited in the Gene Expression Omnibus.

The accession numbers for the microarray data reported in this paper are GSE122925 and GSE122926.